CRYOSMOS

WP200
Scientific Review and Case Studies consolidation
PART 1
WP210 – Scientific review

Requirement Baseline (RB)

Version 1.1 June 25, 2015

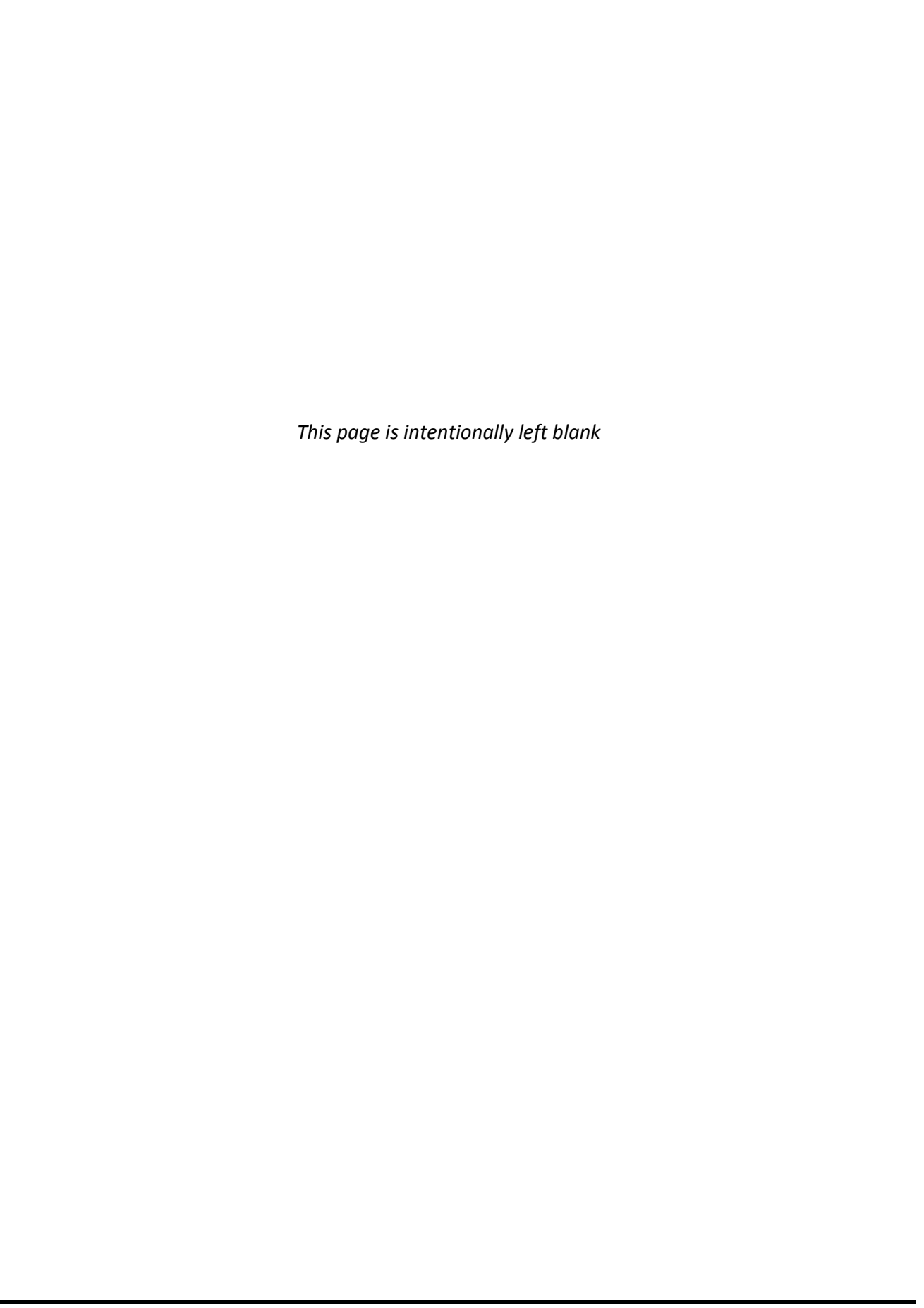




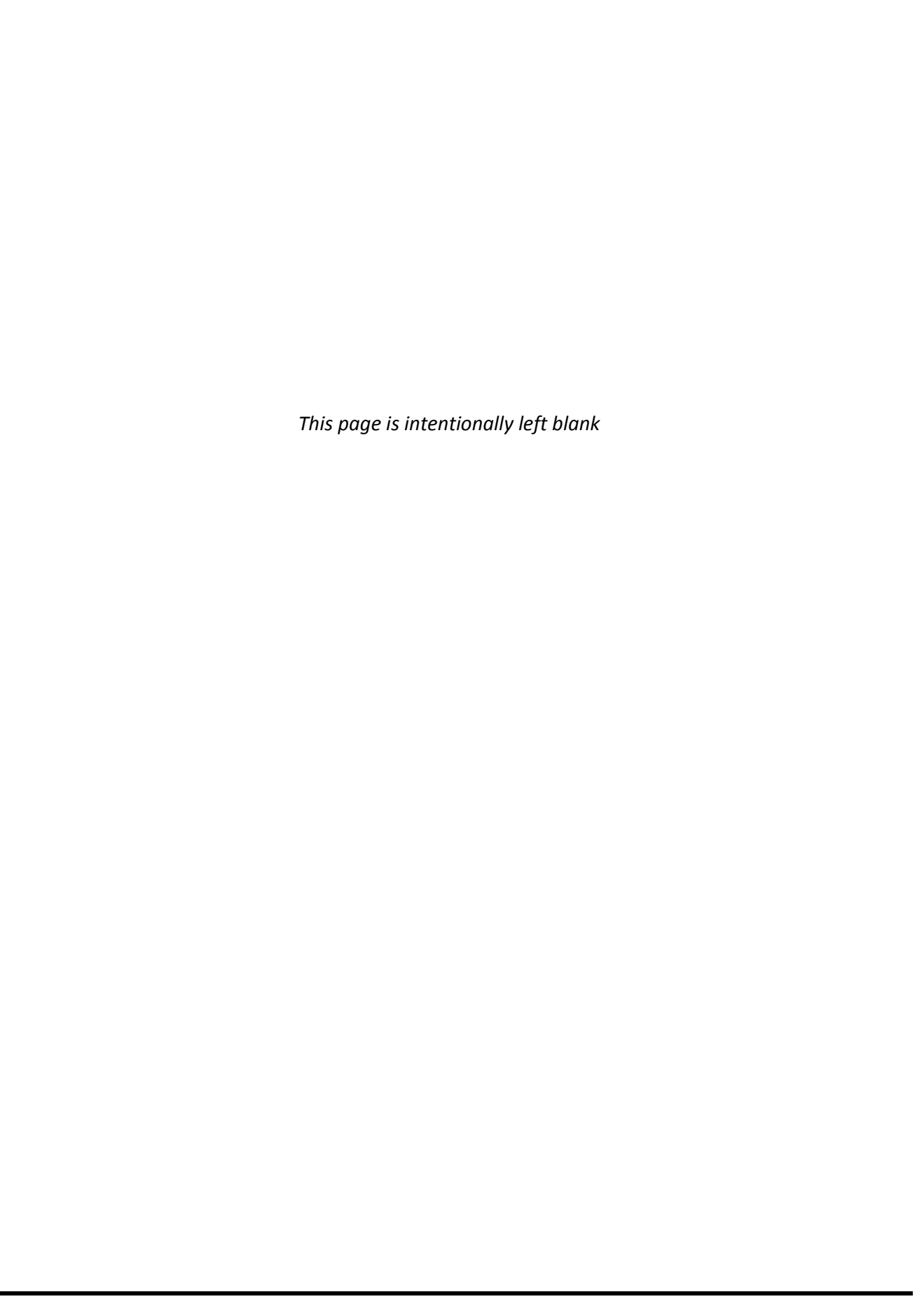








ESA STUDY CONTRACT REPORT			
ESRIN Contract No:	Subject:		Contractor:
4000112262/14/I-NB	CryoSMOS Support To Science Elements SMOS+Cryosphere		IFAC
ESA CR ()No:	Star Code:	No of volumes: 1 This is volume no: 1	Contractor's Ref: Deliverable D1
The work described in this report was done under ESA Contract. Responsibility for the contents resides in the author or organisation that prepared it.			
prepared by: G. Macelloni, M. Brogioni (IFAC), N. Skou, R. Forsberg (DTU), G. Picard, M. Leduc-Leballeur (LGGE), L. Kaleschke (UHAM), A. Mialon (CESBIO).			
ESA STUDY MANAGER: Ola Grabak		ESA BUDGET HEADING	3



DOCUMENT CHANGE LOG

Issue/ Revision	Date	Observations
1/0	03/04/2015	First issue
1/1	25/06/2015	English grammar improved

This page is intentionally left blank	

TABLE OF CONTENTS

1	Pu	rpose and structure of document	9
	1.1	Purpose	9
	1.2	Document Structure	9
	1.3	Definitions and Acronyms	10
	1.4	Reference documents	12
2	Ge	eneral considerations and analysis of existing activities	15
	2.1	Context	15
	2.2	SMOS and Cryosphere	15
	2.3	SMOS and Antarctica	18
	2.4	Background of snow properties studies in Antarctica	22
3	De	scription of suitable electromagnetic models	25
	3.1	Geophysical inputs for model	26
	3.2	First Order Model	29
	3.3	Incoherent model	31
	3.4	Coherent models	33
	3.5	Preliminary results of inter comparison models	35
4	Su	mmary of available associated datasets	38
	4.1	In situ measurements	38
	4.2	Satellites datasets	39
	4.3	Derived products	42
5	Cu	rrent initiatives related to the project	43
6	Re	ferences	45

This page is intentionally left blank	

1 Purpose and structure of document

1.1 Purpose

This document is the Requirements Baseline (RB) document for the CRYOSMOS project. Its propose is to consolidate the scientific requirements and information for implementing the project. The RB will represent the basis for all activities to be carried out during the project.

1.2 Document Structure

The structure of the document is the following (and summarized in Table 1-1 against WPs):

- Section 2 Detailed review and assessment of existing literature, datasets, methods, models and algorithms, as well as related range of validity limitations, drawbacks and challenges of existing approaches relevant for the project.
- Section 3 Description of modeling tools and their appropriateness and relevance to the study as well as their shortcomings or limitations set by knowledge of e-m properties at L-band.
- Section 4 Survey of all accessible associated datasets (space, airborne, in situ) to be used for scientific analysis, development and validation.
- Section 5 Survey of current and upcoming initiatives and projects related to the applications.

Table 1-1: Structure of document against Task work packages

WP	Subtask	Section(s) in this document	Main contributors
200	1	2	All
200	2	3	IFAC, LGGE, UHAM
200	3	4	All
200	4	5	All

1.3 Definitions and Acronyms

Table 1-2 lists the acronyms and abbreviations used within this document.

Table 1-2: Acronyms and abbreviations

Acronym	Meaning
AMSR-E	Advanced Microwave Scanning Radiometer for EO
AMSR-2	Advanced Microwave Scanning Radiometer
AMSU	Advanced Microwave Sounding Unit
CEOS-WGCV	Committee on Earth Observation Satellites-Working Group Calibration and Validation
CESBIO	Centre d'Etudes Spatiales de la BIOsphère
CSCR	Case Studies Consolidation Report
DMRT	Dense Media Radiative Transfer model
DTU	Danish Technical University
ECMWF	European Centre for Medium-Range Weather Forecasts
ECV	Essential Climate Variables
EM	ElectroMagnetic
EO	Earth Observation
EOEP	Earth Observation Envelope Program
EPICA	European Project for Ice Coring in Antarctica
ESA	European Space Agency
GOCE	Gravity field and steady-state Ocean Circulation Explorer
IFAC	Istituto di Fisica Applicata "N.Carrara"
IR	InfraRed
ITT	Invitation To Tender
LGGE	Laboratoire de Glaciologie et Géophysique de l'Environnement
MODIS	Moderate Resolution Imaging Spectroradiometer
MIRAS	Microwave Imaging Radiometer by Aperture Synthesis
ML	Multi-Layer
NIR	Noise Injection Radiometers
NASA	National Aeronautic and Space Administration
QCA-CP	Quasi Crystalline Approximation with Coherent Potential
RB	Requirement Baseline report
SMAP	Soil Moisture Active and Passive mission

Acronym	Meaning
SMOS	Soil Moisture Ocean Salinity mission
SoW	Statement Of Work
SSM/I	Special Sensor Microwave Imager
STSE	Support To Science Elements
ТВ	ТВ
UHAM	University of Hamburg
WALOMIS	Wave Approach for LOw-frequency MIcrowave emission in Snow
WP	Work Package

1.4 Reference documents

[RD1] SMOS ATBD for Level 1 TB [available at: http://www.smos.com.pt/downloads/release/documents/SO-DS-DME-L1PP-0011-ATBD.pdf]

[RD2] SMOS ATBD for Level 2 Soil Moisture [available at: https://earth.esa.int/c/document library/get file?folderId=127856&name=D LFE-1633.pdf]

[RD3] SMOS ATBD for Level 2 Ocean Salinity [available at: https://earth.esa.int/c/document library/get file?folderId=127856&name=D LFE-1505.pdf]

[RD4] Heygster G., Hendricks S., Kaleschke L., Maass N., Mills P., Stammer D., Tonboe R. T., Haas C., 2009, L-Band Radiometry for Sea-Ice Applications, Final Report for ESA ESTEC Contract 21130/08/NL/EL, Institute of Environmental Physics, University of Bremen, November 2009 [available at: http://www.iup.uni-bremen.de/iuppage/psa/documents/smos_final.pdf]

[RD5] Kaleschke L., Maaß N., Haas C., Hendricks S., Heygster G., Tonboe R. T., 2010, A sea-ice thickness retrieval model for 1.4 GHz radiometry and application to airborne measurements over low salinity sea-ice, The Cryosphere, 4: 583-592, doi:10.5194/tc-4-583-2010.

[RD6] Lemmetyinen J. et al., 2011, Technical assistance for the deployment of an X- to Ku-band scatterometer during the NoSREx experiment. Final ESA Study Report, C22671/09/NL [available at: https://earth.esa.int/c/document_library/get_file?&folderId=134665&name= DLFE-1524.pdf]

[RD8] Jezek K. C. et al., 2015, Radiometric Approach for Estimating Relative Changes in Intra-Glacier Average Temperature, IEEE Trans. Geoscience and Remote Sensing, 53(1): 134-143.

[RD9] Kaleschke L., Tian-Kunze X., Maaß N., Mäkynen M., Drusch M., 2012, Sea ice thickness retrieval from SMOS TB during the Arctic freeze-up period, Geophys. Res. Lett., 39, L05501, doi:10.1029/2012GL050916

[RD10] Bell et al., 2002, Origin and fate of Lake Vostok water frozen to the base of the East Antarctic ice sheet, Nature, 416: 307-310.

[RD11] Bell et al., 2011, Widespread Persistent Thickening of the East Antarctic Ice Sheet by Freezing from the base, Science, 331(6024): 1592-1595.

[RD12] Schwank M., Stähli M., Wydler H., Leuenberger J., Mätzler C., Flühler H., 2004, Microwave L-band emission of freezing soil, IEEE Trans. Geosci. Remote Sens., 42(6): 1252–1261.

[RD13] Rautiainen K., Lemmetyinen J., Pulliainen J., Vehviläinen J., Drusch M., Kontu A., Kainulainen J., Seppänen J., 2012, L-Band radiometer observations of soil processes at boreal and sub-arctic environments, IEEE Trans. Geosci. Remote Sens., 50(5): 1483-1497.

[RD14] Mironov V.L., Muzalevskiy K. V., Savin I. V., 2013, Retrieving Temperature Gradient in Frozen Active Layer of Arctic Tundra Soils From Radiothermal Observations in -Band—Theoretical Modeling, IEEE Journal of Selected Topics in Applied Earth Observations and Remote Sensing, 6(3).

[RD15] Lemmetyinen J., 2012, Microwave radiometry of snow covered terrain and calibration of an interferometric radiometer, Aalto University publication series Doctoral Dissertations, 142/2012.

[RD16] Mätzler C., 2006, Microwave dielectric properties of ice. In (Eds. C. Mätzler et al) Thermal Microwave Radiation: Applications for Remote Sensing Chapter 5, IET Electromagnetic Waves Series, Vol. 52, Institute of Engineering and Technology, Stevenage, U.K. SBN: 0-86341-573-3 & 978-0-86341-573-9.

[RD17] Drinkwater M.R., Floury N., Tedesco M., 2004, L-band ice-sheet TB at Dome C, Antarctica: Spectral emission modelling, temporal stability and impact of the ionosphere, Annals of Glaciology, 39: 391–396.

[RD18] Macelloni G., Brogioni M., Pampaloni P., Cagnati A., Drinkwater M.R., 2006, DOMEX 2004: An experimental Campaign at Dome-C Antarctica for the Calibration of Space-Borne Low–Frequency Microwave Radiometers, IEEE Trans. Geosci. and Remote Sens., 44(10): 2642 – 2653.

[RD19] Macelloni G., Brogioni M., Pettinato S., Zasso R., Crepaz A., Zaccaria J., Drinkwater M. R., 2013, Ground-Based L-Band Emission Measurements at Dome-C Antarctica: the DOMEX-2 experiment. IEEE Trans. Geosci. And Remote Sensing, 51(9): 4718-4730.

[RD20] Mätzler C., 2001, Applications of SMOS over Terrestrial Ice and Snow. 3rd SMOS Workshop, DLR, Oberpfaffenhofen, Germany, 10-12 December 2001

[RD21] Søbjærg et al., 2013, DomeCAir C Campaign: EMIRAD Data: Presentation and Analysis, ESA Final Report.

[RD22] Bekaert D., 2011, POLARIS IceGrav Antarctic Campaign 2011. ESA Processed Data Inventory. ESA Tech. Note IPD-ESA-TN-250, Issue 1.2.

This page is intentionally left blank	

2 General considerations and analysis of existing activities

2.1 Context

The idea of using an L-band radiometer by satellite dates from the 1970s. An experiment was designed on American space station Skylab to evaluate the feasibility of monitoring the moisture content of the soil and the ocean salinity from space. The high correlations obtained indicate that microwave sensors may be quite useful for such measurements in the future (Eagleman and Lin, 1976; Blume et al., 1978). Due to the technical complexity at this wavelength, the first satellite using L-band was SMOS (Soil Moisture and Ocean Salinity) launched in 2009, followed by the Aquarius mission in 2011 and the SMAP (Soil Moisture Active and Passive) satellite in 2015.

The main objectives of the SMOS mission which was launched in November 2009 were to measure the surface soil moisture over land [RD2] and the surface salinity of the ocean [RD3]. The instrument is a 2D interferometer that measures the microwave emission of the Earth's surface at L-band (1.4 GHz). The radiometric resolution is about 40km on average, with an ascending/descending orbit at 6am/6pm respectively (solar local time) at the Equator. It covers the entire surface of the Earth within 3 days, thus insuring an interesting time sampling for environmental variables such as soil moisture and ocean salinity. Many applications are being derived from SMOS data, such as a drought index, root zone soil moisture, and assimilation in weather models (ECMWF).

To further exploit and maximise the scientific return of the SMOS mission [RD1], a study of the cryosphere has been clearly identified since the beginning of the mission as a second objective. The cryosphere includes the Earth's surface where water is in solid form, i.e. sea ice, lake ice, river ice, snow cover, glaciers, ice sheets, ice shelves, frozen ground and permafrost. This is an essential element of the global climate system, and requires a detailed understanding and monitoring. SMOS mission offers a new point of view for exploring the cryosphere, thanks to a four-year time series performed at a low microwave frequency that has never used before by a satellite. As observations at microwave frequencies, SMOS gives a very complete time series irrespective of the clouds conditions and without the restriction of daylight (polar nights). However, SMOS differs from higher frequencies by a greater penetration depth in snow (estimated as a few hundred meters at 1 GHz and as a few centimetres at 100 GHz) and a low sensitivity to snow grain size.

Numerous studies have clearly showed the SMOS contribution in obtaining information about sea ice, snow cover, frozen ground, etc. However, studies focused on Antarctica are scarce, and require further investigations. CRYOSMOS project aims to explore the novel capabilities of SMOS to provide innovative observations, new products, and potential future applications within the context of the cryosphere, with special attention to the Antarctic ice sheet, including its floating ice shelves.

2.2 SMOS and Cryosphere

Frozen soil

Changes in the high-latitude annual cycles of soil freezing and thawing and seasonal snow cover have an impact of a highly complex nature on the global hydrological cycle as well as on the release of trace gases and on high-latitude ecosystems. Low microwave frequencies such as L-band have proven to be of interest for frozen areas. Schwank et al. (2004 [RD12], 2014) and Rautiainen et al. (2012 [RD13], 2014) used L-band data to detect the presence of snow and freezing state in the soil. This highlights that the development of freeze—thaw algorithms from current and future L-band satellite missions such as SMOS

and SMAP is highly relevant. The Finnish Meteorological Institute (FMI) indicates that the advance of winter can be closely monitored by means of SMOS observations. During the freezing process, TB increases until the top 50 cm of the soil is frozen. During the winter the TB stay relatively constant, even in the presence of deep snow. Thawing in spring then leads to a decrease in the TB. Figure 1 shows that the extent and depth of frozen soil in northern Finland were considerably greater on 30 November 2011 than four days earlier.

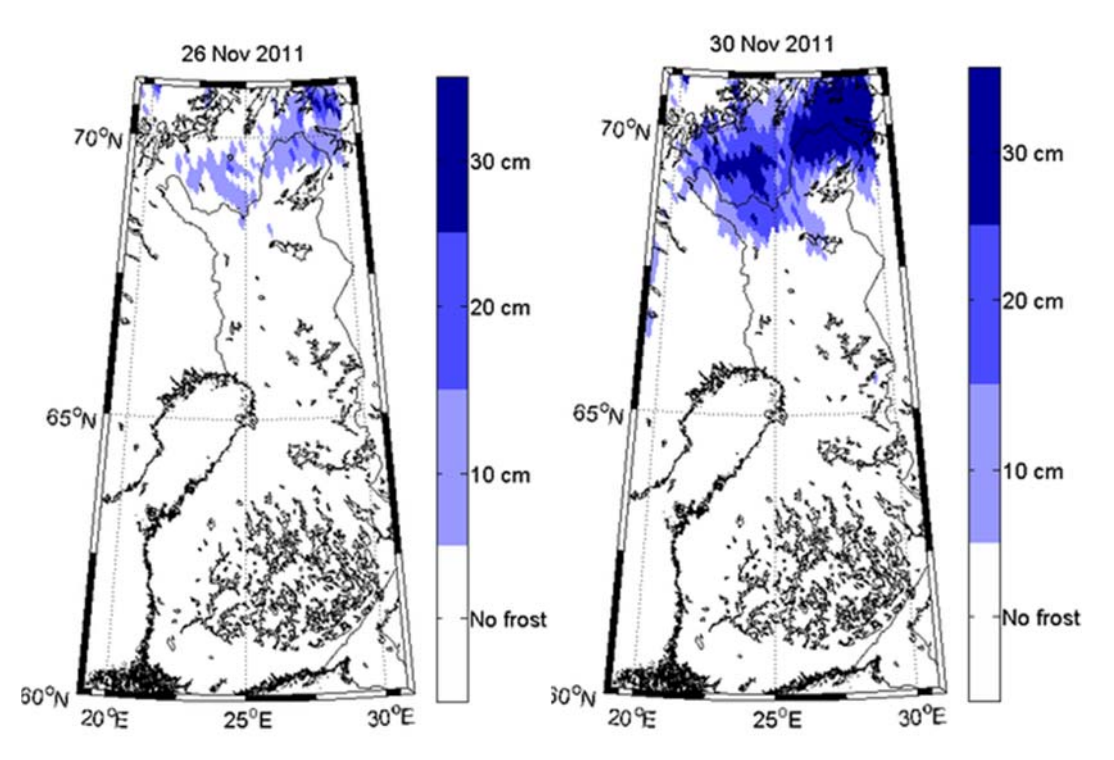


Figure 1: Maps of extend and depth of frozen soil in northern Finland on 26 November 2011 (left) and on 30 November 2011 (right). By K. Rautiainen from Finnish Meteorological Institute (available at: http://www.esa.int/Our_Activities/Observing_the_Earth/SMOS/SMOS_detects_freezing_soil_as_winter_takes_grip)

Recently, Schwank et al. (2014) used a modeling approach and suggested that TB at V polarization measured at around 50° could achieve segregated information on soil-frost. Furthermore, they demonstrated a significant sensitivity of L-band emission at H polarization as compared to the density of the lowest snow layer as a result of refraction and impedance matching by the snowpack. For Arctic soils, Mironov et al. (2010) developed a dielectric constant model at L-band that can be useful for modelling L-band surface emission. Furthermore, Mironov et al. (2013 [RD14]) showed the possibility of reconstructing the surface soil temperature and the surface top-soil temperature gradient. The reconstructed temperature profiles deviated from their in situ measurements by no more than ±0.87°C for the 0.15-cm layer for both the V and H polarizations (Figure 2). The proposed method was especially designed for implementation in the SMOS algorithms in order to derive the temperature of frozen soil and to survey the permafrost areas in the Arctic region.

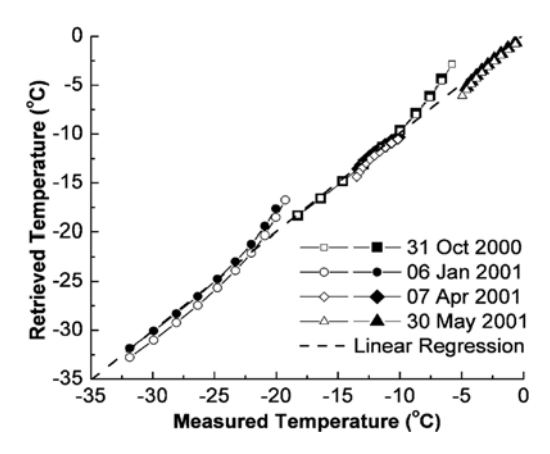


Figure 2: Correlation between the retrieved and measured soil temperatures. The linear regression is the dashed curve. Open and closed symbols correspond to the H and V polarizations, respectively. From Mironov et al. (2013).

Ice thickness

The decline of Arctic sea ice has raised increasing interest in Arctic shipping and the need for operational sea ice forecast systems. Sea ice thickness is one of the key parameters needed for the initialisation of forecast models. It can be derived from the freeboard conversion by using altimetry (e.g. from CryoSat-2) or from microwave radiometry at low frequencies (Kaleschke et al. 2012 [RD9], Ricker et al. 2014). Both retrieval techniques are complementary, because the freeboard method has a large relative uncertainty for thin ice, while the radiometric approach is not sensitive for ice thicker than the penetration depth of the electromagnetic waves in the ice medium (Kaleschke et al. 2010 [RD5]). This maximum ice thickness depends on the liquid brine concentration in the ice and, thus, on the ice salinity and temperature. At the SMOS frequency of 1.4 GHz, the maximum thickness is about half a meter for homogenous level ice. An algorithm based on a combined thermodynamic and radiative transfer model which accounts for variations in ice temperature and ice salinity has been used for the continuous production of a SMOS-based sea ice thickness data product (Tian-Kunze et al., 2014). Its validation so far has been limited to a sparsely available ground truth, and considerable uncertainties have remained (Maaß et al., 2015).

Recently, two field campaigns were conducted in the Barents Sea and in the Beaufort Sea, and obtained a significant amount of new validation data over thin ice. A forecast system for ship route optimisation was recently developed and tested in an operational application during an extensive field campaign with the ice-strengthened research vessel Lance in the Barents Sea, in March 2014. The ship cruise was complemented with coordinated measurements from a helicopter based on the R/V Lance and from the research aircraft Polar 5 operated from Longyearbyen airport, Spitsbergen. Sea ice thickness was measured using an electromagnetic induction (EM) system from the bow of the R/V Lance and from another EM-system towed below the helicopter. Polar 5 was equipped among others with the L-band radiometer EMIRAD2. An array of 15 ice drift buoys was deployed from an aircraft before the ship cruise in order to measure the ice movement. About 80 TerraSAR-X wide-swath mode images were acquired for the main area of investigation between Edgeøya and Kong Karls Land. The experiment yielded a comprehensive data set that makes it possible to evaluate both the operational forecast and route optimisation system, and also the SMOS-derived sea ice thickness product that has been used for the initialization of the forecast. Figure 3 shows two Polar 5 tracks on 24 March 2014 with the UHAM SMOS sea ice product color-coded in the background. The ice thickness derived from the sea ice freeboard measured with the airborne laser scanner (ALS, one minute averages) is shown with colored circles. It can be seen that the gradients of the thick ice region at the coast of Edgeøya are well captured. The ice thickness of the SMOS product is underestimated by about 50% as compared with the ALS thickness, but the SMOS and ALS agree well within the range of their uncertainty.

Furthermore, another airborne campaign in the Beaufort Sea yielded three EM tracks that are partly coincident with CryoSat-2. This recently acquired field data will be used in the ongoing ESA STSE study SMOS+ Sea Ice (PI Lars Kaleschke, UHAM) to further improve and validate the SMOS-based sea ice thickness retrieval and to develop methods for a synergetic sea ice thickness product from SMOS and CryoSat2.

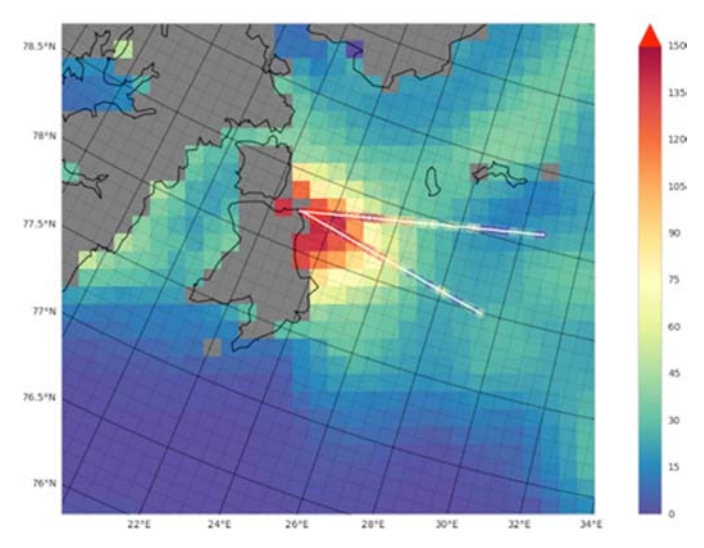


Figure 3: SMOS sea ice thickness (UHAM product) and ALS ice thickness on 24, March 2014.

2.3 SMOS and Antarctica

The annual SMOS TB shows that it is possible to identify several main regions (Figure 4): the internal part where the ice-sheet is always dry, the temperature is very low, and the precipitations are scarce; the coast part, where the snow may be wet, the temperature is higher, and precipitations are more intense and frequent; and the ice-shelf region surrounding the continent.

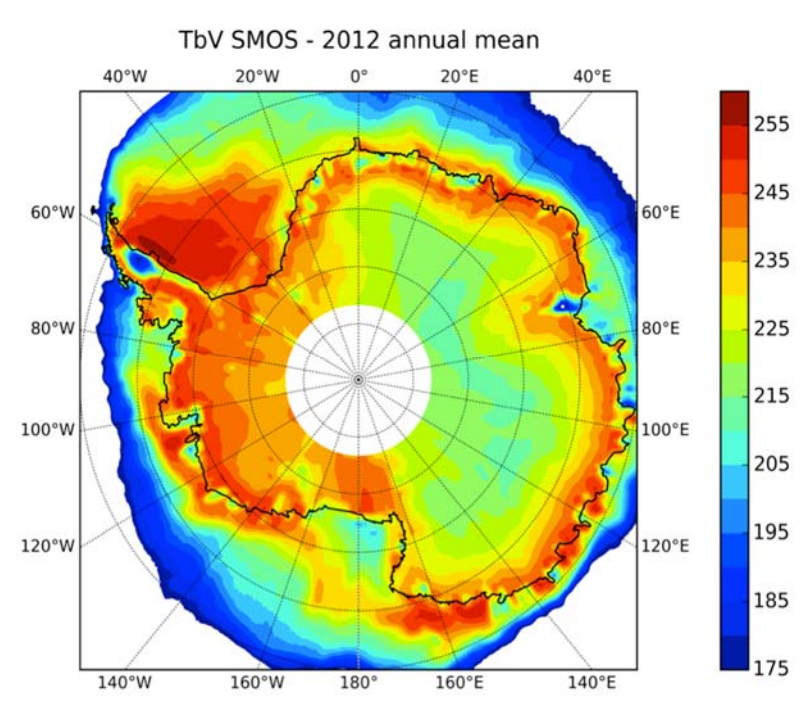


Figure 4: Annual SMOS TB (in Kelvin) at V-polarization at 55° of incidence angle in Antarctica.

Preliminary studies have explored the characteristics of SMOS data with different objectives, and are reported as follows.

Calibration

In recent years, there has been increasing interest on the part of remote sensing community in using the Antarctic area for calibrating and validating data of low-frequency satellite-borne microwave radiometers. Different strategies have been adopted by the various space agencies (Cao et al. 2009) for single missions or sensors, including external calibration and assessment of long-term degradation or drift in sensor performance, which can be determined by using extremely stable natural targets. The identification of suitable calibration and validation (cal/val) sites, the required instrumentation, and long-term deployment and operation provide attractive opportunities for future developments. The Committee on Earth Observation Satellites-Working Group Calibration and Validation (CEOS-WGCV) has identified the need for internationally agreed (CEOS-endorsed) reference sites that should be appropriately instrumented and maintained as a global resource (CEOS-WCGV plan 2011-2016). The ultimate goal for CEOS member agencies would be to agree to collect and provide measurements from all CEOS-endorsed sites in order to facilitate interoperability and to underpin internationally harmonized cal/val activities. Among the possible selections, the East Antarctic Plateau, in particular the area of Dome-C near the Italian-French base of Concordia (located at the top of the dome at 75.06°S, 123.21°E) is being investigated by CEOS as one of the static test sites for a variety of different satellite sensors. The base is located in the middle of the East Antarctic plateau at an altitude of 3280 m above sea level. The site is spatially homogeneous at a 100-km scale and provides extremely limited surface slopes. Moreover, atmospheric conditions are very clear for most of the year, and precipitation is limited. Lastly, the site offers other interesting characteristics that make this area very attractive for the external calibration of remote sensing missions: due to its location, the Dome-C site offers the possibility for observing the area several times per day by means of polar orbiting satellite instruments (depending on sensor characteristics such as orbit, observation mode, swath, observation angle, etc.); detailed information has been obtained from several past campaigns (e.g. bedrock and snow topography, snow accumulation rate, etc.), and several instruments have been installed there for continuous in-situ atmospheric and snow measurements. Thanks to that, cross comparison works by Cabot et al. (2014) have shown that the new versions of SMOS and Aquarius TB are getting close with a bias of less than 1 K.

For the calibration of low-frequency microwave sensors (e.g. SMOS, SMAP, Aquarius), the Dome-C site presents another important and unique attribute. Penetration of microwaves into the layered Antarctic snowpack was estimated by using Ku-band radar scatterometer data (Long and Drinkwater, 2000) and multifrequency model simulations (Macelloni et al., 2007). At Ku-band, the predicted penetration depth is on the order of a few meters, while at P-band it is estimated to be on the order of several kilometres. At L-band, extinction of ice and snow is hundreds of meters, due to the small imaginary part of the snow permittivity, and is influenced very little by the upper part of the firn. Since only the upper ice sheet layers (i.e. down to 10 meters) experience a seasonal temperature variability on the order of 30°C, (below 15 m, the snow temperature does not exhibit any significant seasonal temperature variation greater than 0.5°C), the expected yearly variability in TB is extremely small (less than 1 K).

Starting from 2004 different campaigns, named DOMEX-1, DOMEX-2 and DOMEX-3, which are based on the ground based L-band radiometer RADOMEX, have been carried out at Dome C in the East Antarctic Plateau (Macelloni et al. 2006 [RD18], 2013 [RD19]). The latter experiment started in December 2012, and is still on-going. The main aim of these experiments was to measure the TB of the area at L-band at different timescales (from 1 month up to several years) and thus to assess its temporal stability. Moreover DOMEX data were compared with SMOS and airborne data collected in the same area (Søbjærg et al., 2013 [RD21]). The analysis of the temporal trend of DOMEX data, collected at 42°

incidence angle, demonstrated the high stability of the TB at L-band, in particular the V polarization, which exhibit an annual standard deviation of around 0.5 K. The H polarization data were more variable, exhibiting a standard deviation of around 1.5 K. The results are similar to reports in other papers at higher frequencies (Picard et al., 2009; Sherjal and Fily, 1994; Surdyk, 2002; Macelloni et al., 2007), and are due to the fact that H polarization is more sensitive to modification of snowpack layering and surface properties.

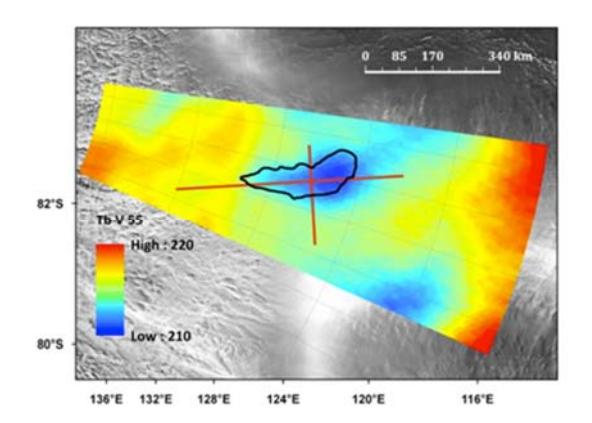
Snow temperature

A recent paper by Jezek et al. (2015 [RD8]) investigated the possibility of retrieving temperature profile using an innovative technique based on a multi-frequency microwave radiometer. The TB for thick polar ice was modelled by using a first-order model (cf. section 3.2). The results demonstrated that TB are sensitive to relative changes in the average ice sheet internal temperature at depth. Moreover, it was demonstrated that by using dielectric properties of the ice sheet that are consistent with the literature, the emission over the entire depth of the ice sheet, which is about 3000 m thick, can potentially contribute to the integrated signal at lower frequencies (i.e. lower than 1 GHz). At these frequencies, an unfrozen ice sheet base showed a signature associated with the changing electromagnetic boundary condition. Such information, whether it be from the upper tens of meters of the ice sheet or from the deepest regions, is crucial for improving glacier dynamics models.

In the same paper, SMOS data over Lake Vostok were analyzed and related to the ice sheet thickness. SMOS Level 1C product obtained from the Operational Processor (L1OP) version V5.05 was used from January to February 2012. This product is resampled to a fixed grid (ISEA 4H9) with a spatial resolution between the nodes (also called DGG = Digital Global Grid) of about 15 km. The 1.4 GHz vertically and horizontally polarized SMOS data near an incidence angle of 25° and 55° were interpolated using an inverse distance weighting scheme (Figure 5) and were overlaid on a Radarsat C-band image mosaic with a polar stereographic projection. The bright radar regions extending away from the lake location were associated with higher backscattering from the ice divide where the accumulation rate is low. The location of the ice divide is correlated with cooler TB. However, it should be noted that the coldest TB were observed within the known boundary of the lake (Jezek et al., 2012; Brogioni et al., 2013).

Figure 6 illustrates horizontally and vertically polarized TB at incidence angles of 25° and 55° extracted along the south-to-north and west-to-east lines shown in Figure 5. In the same figure, the total ice thickness (Fretwell et al., 2013) is also shown along a transect. As expected, V-polarized TB are warmer than H-polarized TB because of differences in the reflection coefficient. At the low incidence angle, the TB anomaly for each transect is almost the same at V and H polarization and the TB trend shows a good correlation with the ice thickness. The east/west anomaly is about 5 K at 25° incidence angle and around 4.5 K at 55° incidence angle at both polarizations. The south/north profiles trend perpendicular to the ice divide and so traverses changing glacial regimes. Consequently the TB anomaly is larger than in the previous case and reached more than 10 K for all incidence angle and polarization except for V polarization and 55° of incidence angle where it exhibits a value of 5 K. Near surface variability in scattering along the north south profile is evident from SAR imagery which consistently shows the ice divide to be a relatively stronger, more homogeneous scattering region than the surrounding parts of the ice sheet. The west/east line runs more nearly parallel to the ice divide and may be less susceptible to changes in surface physical properties such as firn density and grain size, which change with distance from the divide. Consequently, we suggest that the 4-5 K TB anomaly over the lake and along the west/east line, which was observed by both polarization and both incidence angles better captures subsurface information and ice thickness differences.

These results suggest that there may be a correlation between deep ice sheet physical temperatures and SMOS TB.



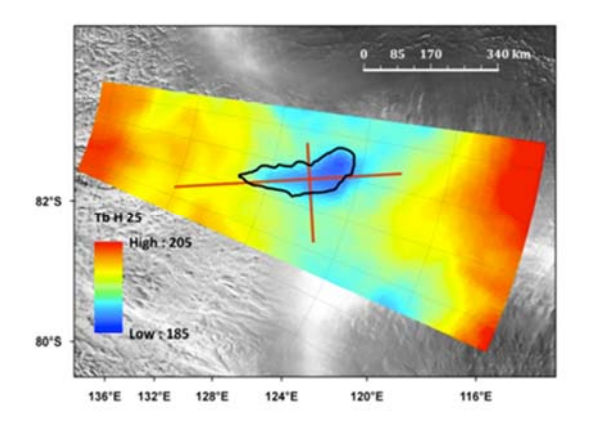


Figure 5: SMOS vertically polarized data at 55° incidence angle (left) and horizontally polarized data at 25° incidence angle (right) over Lake Vostok (outlined in black) in early 2012. There is a weak indication of a cold TB anomaly correlated with the lake location. Red lines depict the locations where TB profiles were extracted (shown in Figure 6). The north/south transect runs from right to left, while the east/west transect runs from top to bottom. From Jezek et al. (2015 [RD8]).

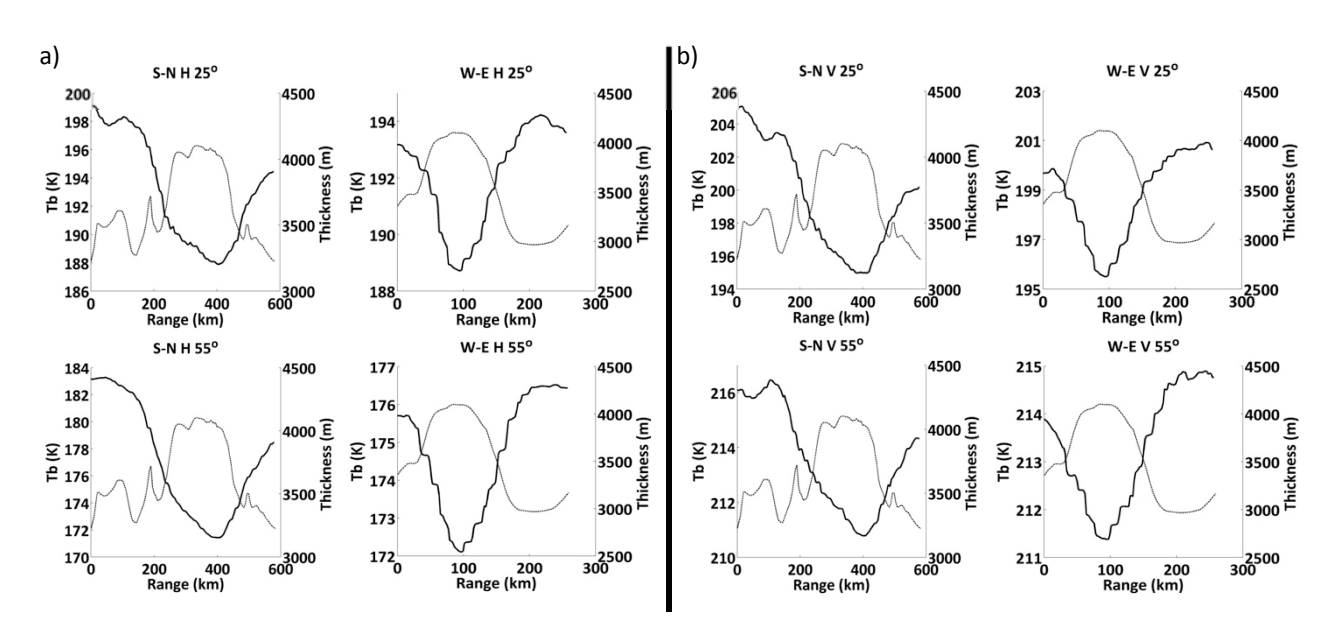


Figure 6: SMOS TB at (a) vertical and (b) horizontal polarisations (heavy, black curves) at 25° incidence angle (upper panels) and at 55° incidence angle (lower panels) along transects going from south to north (sn) (left panels) and west to east (we) (right panels) profiles shown in Figure 5. The intersection of the west/east and the south/north profiles occurs at about 320 km along the south to north profiles and about 90 km on the west/east profiles. Ice thickness (Fretwell et al., 2013) is shown by the thinner gray line. After Jezek et al. (2015 [RD8]).

Bedrock Topography

A 350 x 350 km area near the Concordia station on the high plateau of Dome C in Antarctica was in the DOMECair campaign mapped by an airborne L-band radiometer system and a gravimeter. The area was expected to display a rather uniform TB close to the yearly mean temperature — well suited for calibration checks for space-borne instruments such as SMOS, Aquarius, and SMAP. The measured TB shows unexpected variations: for example, the 8 K variation on an East-West profile through Concordia, and in certain cases a slope of almost 1 K per km (Skou et al., 2013). A convincing correlation was revealed when comparing the measured TB map with bottom topography reveals. Simple simulations show that variations in bedrock topography can indeed modulate the TB in a way that is appropriate for explaining the observed variations (Skou et al., 2014).

2.4 Background of snow properties studies in Antarctica

TB acquired at higher microwaves frequencies (6-89 GHz) by SSM/I, AMSU or AMSRE sensors are sensitive to various layers of the snowpack due to their penetration depths, which depend on the wavelength (about 20 m at 6 GHz and few centimetres at 100 GHz). These instruments have been widely used to retrieve information regarding Greenland and Antarctica ice-sheets. The following sections present an overview of the activities performed using these sensors.

Snow temperature

Microwave measurements are related to the temperature of the observed target, but the conversion from microwave emission to snow temperature is not simple and greatly depends on the emissivity through snow properties. Moreover, since the temperature and emissivity of snow change as a function of depth, the relationship between measured brightness temperature and temperature is thus not simple, and depends considerably on frequency. Surdyk (2001) suggested that TB at 37 GHz and V polarisation can provide a very useful estimate of air temperature changes, because penetration into the ice sheet at this frequency is limited (i.e. less than 1 m). However, these TB cannot be interpreted as a pure surface temperature signal, because the variability in microwave emissivity is not known. Attenuation of surface temperature changes through the penetration depth of the microwave emission—typically a few centimetres to one meter—means that the amplitude is generally smaller for TB variations than for air temperature variations (Picard et al., 2009). Schneider et al. (2004) suggested an approach, that is based on both TB from microwave and on IR frequency. Nevertheless, biases in the IR TB which are associated with cloud cover, and in the microwave TB, which are associated with attenuation and possible emissivity changes, have not been completely removed in this study. The measurement of the snow temperature below 1 m using a passive system has not yet been treated.

Clear-sky land surface temperatures (LST) are derived from observations of the MODIS instruments. This product was evaluated by Wan (2014) using the radiance-based method, which found a LST error of only -0.5 K for the South Pole site. The accuracy of the MODIS LST depends primarily on the quality of the detection of clouds. However, Fréville et al. (2014) showed that MODIS LST can be used as a precise and accurate reference for testing other surface temperature data sets.

Accumulation rate

Accumulation rates are essentially equivalent to the meteorological "surface mass balance," i.e. the net mass flux from atmosphere to ice. Maps of accumulation rate have been derived from compilations of data collected in situ from snowpits, snow-stakes, or ice cores, sometimes augmented by satellite observations (e.g. Vaughan et al., 1999). Arthern et al. (2006) mapped the variations in the mean annual

snow accumulation across the Antarctic ice sheet by using the AMSR-E on the Aqua satellite. This radiometer operates at 6.9 GHz, which corresponds to a wavelength of 4.3 cm in free space and measures TB at V and H polarisations with an incidence angle of 55°. The authors observed that the polarization varies with the accumulation rate according to an inverse square power law, and provides an accumulation map of Antarctica with an effective resolution about 100km. Magand et al. (2008) showed the limits of this approach in the wet zone.

Grain size

In Antarctica, albedo is a key parameter for following the changes in the polar climate. Surface grain size can be used to estimate albedo, and higher microwave frequencies are thus useful due to their high sensitivity to grain size and low penetration depth in snow. Therefore, to explore the grain size profile in the dry snow area of Antarctica, Brucker et al. (2010) analysed emissivities of 37 and 19 GHz channels at V polarisation from SSM/I satellite. From a modelling study, they showed that an overall increase in the snow grain radius with depth is required in order to match the observed emissivity in Antarctica. Moreover, they were able to retrieve two parameters: the near-surface grain radius (representative of the grain radius in the top few decimetres), and the vertical gradient of the grain radius. In the same way, Picard et al. (2012) obtained information on grain size from a grain index based on TB at 89 and 150 GHz collected by the Advanced Microwave Sounding Unit B (AMSU-B). Grain index is intended to increase as the grain size increases.

Surface state

Hoar crystals episodically cover the snow surface in Antarctica and affect the roughness and reflective properties of the air—snow interface. Champollion et al. (2013) investigated hoar evolution at Dome C in Antarctica using continuous observations of the surface by means of in situ near-infrared photography and of passive microwave remote sensing. The authors defined a daily indicator of the presence/absence of hoar crystals from photography data and found a frequency of hoar presence as high as 40% at Dome C. In addition, they showed a correlation with the microwave polarisation ratio: i.e. high values of polarisation ratio, which theoretically correspond to low snow density values near the surface, are associated with the presence of hoar crystals in the photography data. Satellite data over nearly ten years (2002–2011) have confirmed that a strong decrease in the polarisation ratio (i.e. signature of hoar disappearance) is associated with an increase in wind speed or a change in wind direction from the prevailing direction.

In the same way, with L-band measurements from DOMEX campaign Macelloni et al. (2013 [RD19]) also observed a significant correlation between the H-polarization variations and the "strong wind" events (wind speed exceeded 7 m/s for several hours) registered by the AWS (Automatic Weather System) at Dome C. It was supposed that these events are capable of modifying the vapor and heat fluxes in the firn and, hence, the top meter of the snowpack. These events were followed by quiet periods during which modifications in the snow structure were by comparison very slow, and the TB signal remained more stable. Another paper (Brucker et al., 2014) related the modification in the TB at H polarization as observed by NASA's Aquarius sensor to periods of several weeks with hoar on the surface. These aspects could be analysed in depth within this project.

Picard et al. (2014) investigated spatial variations of TB around Dome C at the metre-to-kilometre scale. They found significant variations at 37GHz up to 10K, with a semi-periodic structure that had a scale length of 30-40m. Using modeling and observations, the authors found that snow density was the main factor explaining these variations and that the latter were closely related to snow dunes formed by wind. The variations decreased with the frequency at the investigated frequency (37, 19 and 11 GHz), which suggested that they should thus be negligible at L-band.

Melting

Passive and active microwave remote sensing is sensitive to surface melting, i.e. the presence of liquid water in the first meter of firn. Detection is based on the large difference between the dielectric constants of ice and water in the microwave domain. For the Greenland ice-sheet, Abdalati and Steffen (1997) used 19 and 37 GHz satellite channels (from SMMR and SSM/I) to propose a melt-detection algorithm based on the cross-polarized gradient ratio (XPGR) with an empirical threshold. However, the XPGR seemed to work well for intense melting but did not give good results elsewhere. Thus, in Antarctica, Torinesi et al. (2003) chosen the 19-GHz channel at H polarization to detect onsets of the melt. Given that melt induces large increases in TB, an annually and regionally varying threshold is calculated and all values of TB above the annual mean plus this threshold are associated with melting. This threshold is proportional to the standard deviation of the signal, thus taking into account the spatial variability of its amplitude. Based on Torinesi et al. (2003), the algorithm of Picard and Fily (2006) extended the existing data set of surface melting in Antarctica up to 26 years (1979-2005) with a correction of the overpass-time of the difference sensors. Figure 7 shows the number of days with surface melt during 2012-2013.

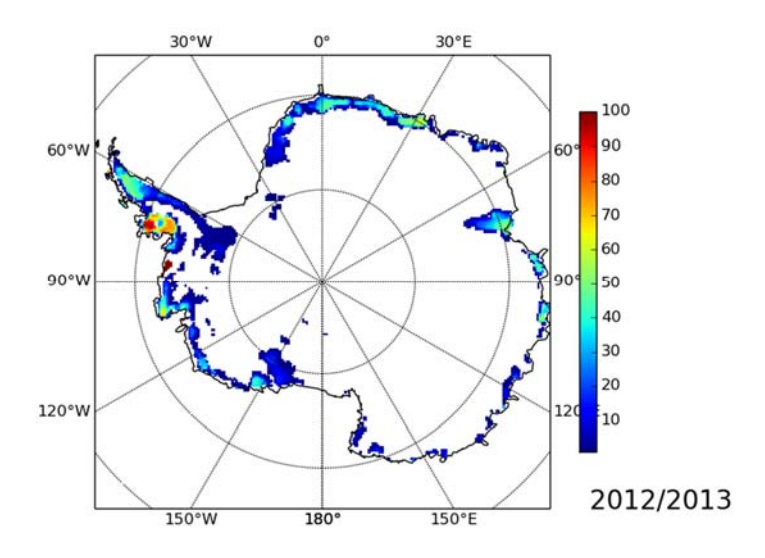


Figure 7: Number of days with surface melt in 2012/2013, retrieved from Picard and Fily (2006; http://www-lgge.obs.ujf-grenoble.fr/~picard/melting/).

Since 2011, Aquarius mission has given an L-band TB with a spatial resolution of around 100km (Lagerloef G. et al., 2008), which is greater than that of SMOS (around 44km). However, recent studies have clearly shown the advantages of L-Band TB for retrieving information on snow surface properties in Greenland and Antarctica. Brucker et al. (2014b) explored the 2012 summer during which almost the entire Greenland ice sheet, including Summit, simultaneously experienced surface melt (e.g., Nghiem et al., 2012; Hall et al., 2013). Thanks to the small attenuation of the L-band radiation in dry snow and ice, satellite L-band observations at Summit showed that there was no annual cycle related to seasonal variations in the snow temperature profile (Figure 8). However, observations in the summer are impacted by snow melt. The melt event of the 2012 summer formed a refrozen snow layer, and thus led to a sustained decrease in the L-band TB of about 5 K at H polarization (Figure 8; Brucker et al., 2014b). Such a dramatic change in the L-band TB level revealed the impact of the recently formed near-surface refrozen snow layer on TB. Although melting events do not occur in the inner part of the Antarctic plateau, the above result confirms that, whereas the L-band radiation emanates from deep within the

ice sheet, modifications in the snow properties near the surface (e.g. density variation) do indeed influence L-band observations. These aspects could be analysed in depth within this project.

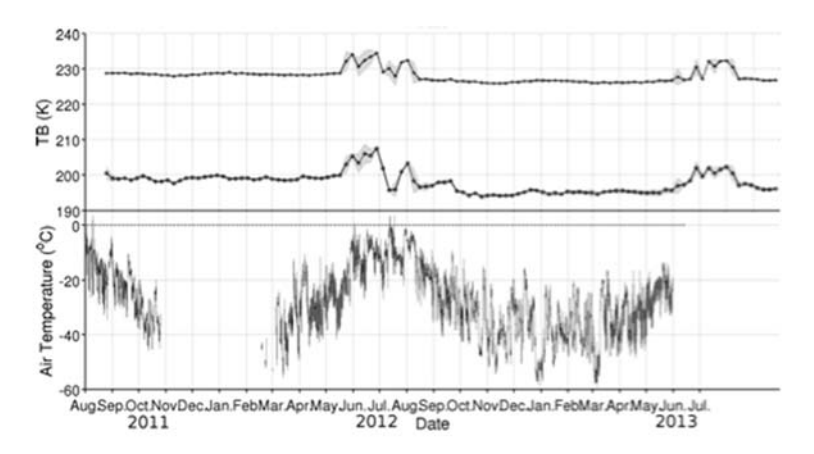


Figure 8: Aquarius time series of TB (radiometer 1, incidence angle 29°) at V (+) and H (o) polarizations, and GC-net air temperature measurements over Summit (Greenland). The grey area corresponds to the weekly TB standard deviation. From Brucker et al. (2014b).

3 Description of suitable electromagnetic models

Modelling is a useful means for evaluating the sensitivity of SMOS signal to a given parameter, and will be widely used to explore chosen case studies.

Several models are available for computing the microwave emission from given snow properties, and different approaches have been developed. Nevertheless, these models were developed and tested for simulating the microwave emission of snow on land or, in the case of ice sheets, were validated at higher frequencies only, and their applicability to L-band or lower frequencies has been investigated only recently. (Jezek et al. 2015, Leduc-Leballeur et al. 2015, Tan et al. 2015). In this section an overview of available models described in these and others papers will be provided. An initial section is devoted to the representation of the medium, that is fundamental to provide reliable inputs to the e.m. models.

3.1 Geophysical inputs for model

In e.m. models, the polar ice sheet structure is approximated as a planar layered medium in which each layer is characterized by physical properties such as temperature, density, and grain size (Figure 9).

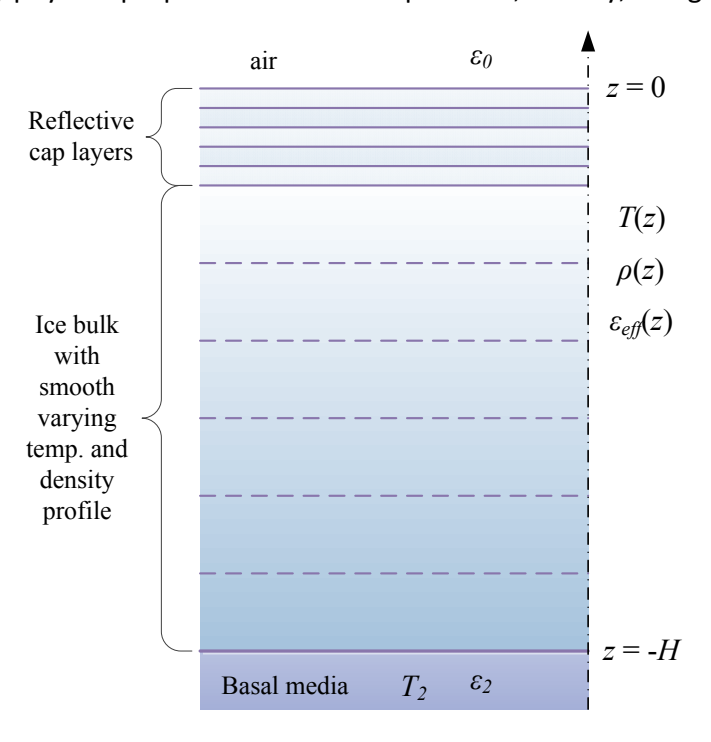


Figure 9: Illustration of the vertical structure of the polar ice sheet. From Tan et al. (2015).

The definition of these input parameters is a key point in the simulation of the L-band TB. They are dependent on geophysical characteristics of the medium, that could be obtained from experimental measurements or glaciological models. Some of these quantities are related to surface and sub-surface characteristics (i.e. surface roughness, characteristics of the layers, snow density and temperature, grain size and shape etc.) that are, in certain cases, available from field measurements, while others depend on physical properties of the ice sheet as a function of depth, and are obtained from other ancillary measurements or derived from glaciological models.

At Dome C (Antarctica), in situ measurements were carried out during the austral summer campaign of 2012–2013, with a focus on long ice-core and high vertical resolution measurements (5cm). Two cores were 80 m long, corresponding to the ice sheet part, where the density is most variable (Figure 10). These measurements gave a very detailed description of snowpack, and were very useful for studying the L-band modelling in this area (Leduc-Leballeur et al., 2015).

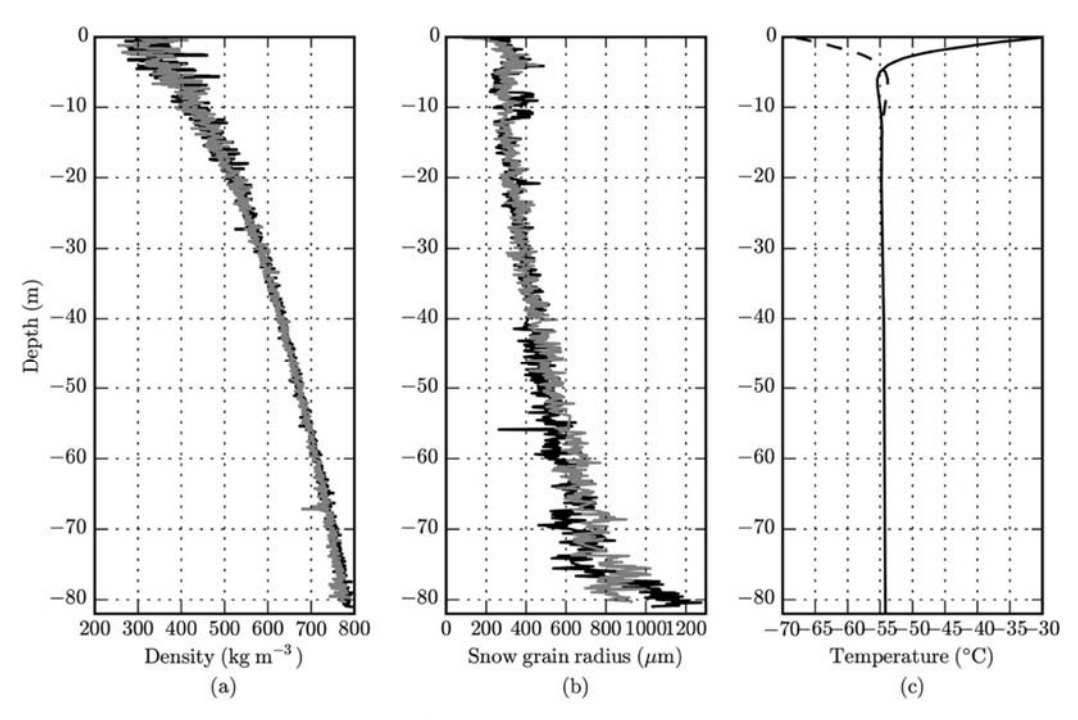


Figure 10: Profiles of (a) snow density (kg m⁻³) and (b) grain size (μm) measured on two ice cores, at Dome C, in Antarctica during the 2012–2013 austral summer. (c) Mean temperature profiles (°C) were measured in January (solid line) and July (dashed line). From Leduc-Leballeur et al. (2015).

However, ice cores are not available over the entire continent and it is usually necessary to use glaciological models in order to estimate snow properties (Jezek et al., 2015 [RD8]).

Ice sheet temperature generally increases with depth, except for the very top layers (about 10 meters) where the seasonal swing in the air temperature alters the ice temperature (Macelloni et al., 2013 [RD19]; Bringham and Drinkwater, 2000; Drinkwater et al., 2004 [RD17]). Since the top layers contribute little to the ice-sheet thermal emission at low frequencies, the near surface seasonal temperature variation can be disregarded (Leduc-Leballeur et al., 2015) and the temperature profile T(z) can be estimated by following Robin (Van der Veen, 1999; Jezek et al., 2015 [RD8]):

$$T(z) = T_s + C \cdot \operatorname{erf}\left(\frac{H}{L}\right) - C \cdot \operatorname{erf}\left(\frac{z+H}{L}\right), -H \le z \le 0$$
 (1)

where $C=\frac{LG\sqrt{\pi}}{2k_c}$ and $C=\frac{LG\sqrt{\pi}}{2k_c}$, $\operatorname{erf}(\cdot)$ is the error function, $T_s=T(0)$ is the surface temperature, M is the ice accumulation rate, measured in meters-per-year ice equivalent, and H is the overall ice thickness. $G=0.047W\cdot m^{-2}$ is the geothermal heat flux, $k_c=2.7W\cdot m^{-1}\cdot K^{-1}$ is the ice thermal conductivity, and $k_d=45m^2\cdot \mathrm{yr}^{-1}$ is the ice thermal diffusivity. Two temperature profiles are illustrated in Figure 11(a) for $T_s=216K$, H=3700m with M set to 0.01 and 0.05 $m\cdot \mathrm{yr}^{-1}$. These values are generally representative of the deep interior East Antarctic ice-sheet. The lower ice accumulation rate corresponds to the higher temperature. Moreover, equation (1) is applicable when the ice sheet movement is negligible; otherwise, it must be modified as explained in the D2 report.

The average firn density $\rho(z)$ increases with depth (Alley et al., 1982; Bingham and Drinkwater, 2000; Drinkwater et al., 2004 [RD17]). By following the measurement of Alley et al. (1982), $\rho(z)$ can be defined by:

$$\rho(z) = 0.922 - 0.564 \cdot \exp(0.0165z) \ g/cm^3$$
 (2)

The near surface density fluctuation $\tilde{\rho}(z)$ is modeled as the sum of the average density $\rho(z)$ and a damped noise $\rho_n(z)$:

$$\tilde{\rho}(z) = \rho(z) + \rho_n(z) \cdot \exp(z/\alpha) \tag{3}$$

with α as a damping factor, as previously proposed in Brogioni et al. (2014). Unlike Brogioni et al. (2014), however, since the fluctuation is spatially correlated, the noisy part $\rho_n(z)$ is modeled as a Gaussian random process with the Gaussian correlation function given by $\langle \rho_n(z)\rho_n(z')\rangle = \Delta^2 \exp\left(-\frac{(z-z')^2}{l^2}\right)$, where Δ^2 is the auto-covariance and l is the correlation length (Brogioni et al. (2014) assumed l=0). A random realization of density fluctuations with $\alpha=30m$, $\Delta=0.040 {\rm g/cm^3}$, and l=10cm is illustrated in Figure 11(b). Leduc-Leballeur et al. (2015), following West et al. (1996), modelled the profile with an autoregressive model of order 1 (AR(1)) in order to representation the local variations.

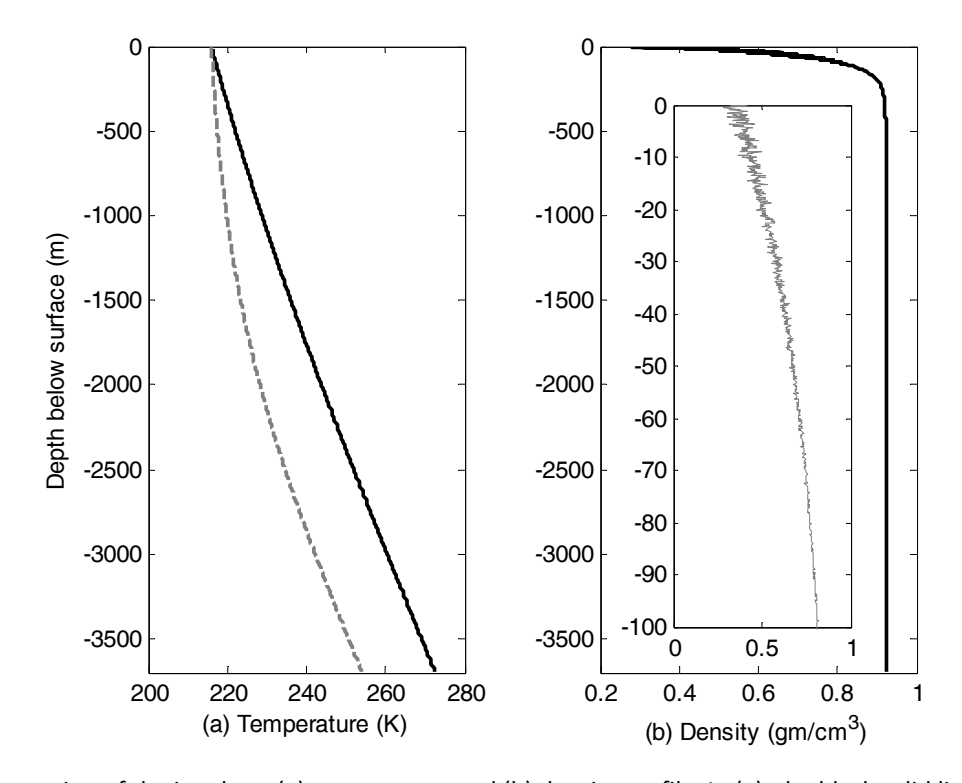


Figure 11: Illustration of the ice sheet (a) temperature and (b) density profile. In (a), the black solid line corresponds to $M=0.01m\cdot {\rm yr^{-1}}$, and the grey dashed line corresponds to $M=0.05m\cdot {\rm yr^{-1}}$. The small insert in (b) shows the density fluctuations in the top 100 meters modeled by a damped Gaussian random process. The density profile is specified by $\alpha=30m$, $\Delta=0.040g/cm^3$, and l=10cm. From Tan et al. (2015).

The grain radius profile a(z) can be estimated by following Zwally's (1977) fit to Gow's (1971) parameterization of Plateau station grain size between 0.5m and 71m:

$$a(z) = \sqrt[3]{0.0377 + 0.00472|z|}mm \tag{4}$$

with z in meters. The volume scattering is confined to the top 90m of the ice sheet by considering the near-homogeneous ice composition below this depth (Jezek et al., 2015 [RD8]). Brucker et al. (2010) provided an indirect method for estimating grain size profiles in the top 10m from high frequency observations (19 and 37 GHz).

The material beneath the ice sheet can be either frozen rock (relative permittivity 5 + 0.1i; Ulaby et al., 1990) or liquid water (80 + 79i; Stogryn, 1971), depending on the basal temperature. When the basal

temperature approaches the melting point of ice, sub-glacial water at 273K is assumed at the basal boundary; otherwise, an isothermal semi-infinite sub-glacial layer of frozen rock at the same temperature as that of the bottom of the ice sheet is assumed (Jezek et al., 2015 [RD8]).

The above description is applicable to the inner part of the ice sheet although different density, grain size and temperature profiles must be applied when areas near to the coast are considered.

Moreover ice shelves present a completely different structure. For example, as the ice shelf floats on the ocean, we can assume a well-defined permittivity of sea water for the bottom layer of the radiative transport (Klein and Swift, 1977). The situation is more difficult when there is a possible layer of marine ice below the ice shelf. There are no direct measurements or models of the marine ice layer permittivity but some information is available regarding the salinity, which may be comparable to brackish sea ice. Thus, we will assume the existing parameterizations for Baltic Sea ice in order to describe the marine ice layer (Kaleschke et al., 2010 [RD5]).

3.2 First Order Model

The first order RT model is derived from the radiative transfer equation bu disregarding the source term from scattering (Jezek et al., 2015 [RD8]; Zwally, 1977; Tsang et al., 1985; Swift et al., 1985). It also disregards all intermediate reflections inside the ice sheet, including reflections from the top air/snow interface and bottom ice/base interface only. It assumes that the scattering coefficient (k_s) is small as compared to the absorption coefficient (k_a) , which is realistic at L-band in most conditions. The physical temperature in the material beneath the glacier base is assumed to be constant and equal to the temperature of the bottom of the ice. The equation can be applied for either an isothermal, semi-infinite sub-glacial layer of frozen, rock-base, or for a liquid water-base, depending on the basal temperature. For the sake of simplicity, the model is described for normal incidence (i.e. nadir) radiometric observations. A more complete formulation, which is described in Tsang et al. (1985), is capable of addressing arbitrary observation angles and polarization effects.

TB in nadir can be approximated by

$$T_{b} = \left(1 - r_{air/snow}\right) \left[\int_{-H}^{0} dz T(z) \kappa_{a}(z) \exp\left(-\int_{z}^{0} dz' \kappa_{a}(z')\right) + \left(1 - r_{ice/base}\right) T_{base} \exp\left(-\int_{-H}^{0} dz' \kappa_{e}(z')\right) \right] + r T^{Sky}$$

$$(5)$$

where T(z) is the temperature profile, and $\kappa_e(z) = \kappa_a(z) + \kappa_s(z)$, with $\kappa_a(z)$ and $\kappa_s(z)$ as the absorption coefficient and scattering coefficient at depth z, respectively. The first term in brackets represents the emission from the icy medium. The second term represents the emission from the basal media attenuated by all the ice layers, where T_{base} is the physical temperature of the base. $r_{air/snow}$ and $r_{ice/base}$ are the reflectivities between the air/snow interface and ice/base interface, respectively. At nadir, $r_{air/snow}$ is typically 0.016 and $r_{ice/base}$ is 0.012 for frozen rock base and 0.46 for water base. In equation (5) the last term accounts for the sky radiation reflected by the surface and subsurface, where the solar and galactic radiation T^{Sky} depends on the polar sun elevations, which vary from place to place and day-of-year etc., and the surface reflectivity r depends on assumptions regarding the density profile.

To compute the absorption and the scattering coefficient, it is necessary to define the effective permittivity of the medium in its real and imaginary parts. The real part of the effective permittivity $\varepsilon'_{r,eff}$ of the ice layer is calculated by unsing Mätzler's empirical formula (Wiesmann et al., 1999; Mätzler, 1996), while the imaginary part $\varepsilon'_{r,eff}$ is calculated by following the Tiuri et al. (1984)'s empirical model for dry snow:

$$\varepsilon'_{r,eff} = 1 + 1.4667 f_v + 1.435 f_v^3, 0 < \rho \le 0.4g/cm^3$$
 (6)

$$\varepsilon_{r,eff}' = [(1 - f_v)\varepsilon_h^b + f_v\varepsilon_S^b]^{1/b}, \rho > 0.4g/cm^3$$
(7)

$$\varepsilon_{reff}^{"} = \varepsilon_{rice}^{"}(0.52\rho + 0.62\rho^2) \tag{8}$$

where:

 ρ is the snow/ice bulk density,

 $f_v = \rho/(0.917g/\text{cm}^3),$

 $\varepsilon_h = 0.9974$,

 $\varepsilon_s = 3.215$,

b = 1/3,

 $\varepsilon_{r,ice}^{\prime\prime}$ is the imaginary part of the ice permittivity.

The complex dielectric constant of ice $\varepsilon_{r,ice} = \varepsilon'_{r,ice} + i\varepsilon''_{r,ice}$ is calculated by following Mätzler (2006 [RD16])'s semi-empirical model, which predicts an increasingly imaginary part of the relative permittivity as the temperature is increased.

The effective permittivity of the ice layer is then used to calculate the absorption and scattering coefficients by using the QCA-CP of non-sticky spheres (Tsang and Kong, 2001):

$$\kappa_a = k_0 \varepsilon_{r,eff}^{\prime\prime} / \sqrt{\varepsilon_{r,eff}^{\prime}} \tag{9}$$

$$\kappa_{s} = \frac{2}{9} k_{0}^{4} a^{3} f_{v} \left| \frac{\varepsilon_{ice} - \varepsilon_{0}}{1 + \frac{\varepsilon_{ice} - \varepsilon_{0}}{3\varepsilon_{eff}} (1 - f_{v})} \right|^{2} \frac{(1 - f_{v})^{4}}{(1 + 2f_{v})^{2}}$$
(10)

where a is the grain radius, and k_0 is the free space wave number.

As the density increases, the f_v tends to 1 and the scattering coefficient is extinguished. For example, at the SMOS frequency, Jezek et al. (2015 [RD8]) computed this term as a function of depth for a density profile typical of the internal part of the East Antarctic Plateau (Figure 12). It could be observed that, from around 90 m, the scattering term is negligible and could be omitted from this depth.

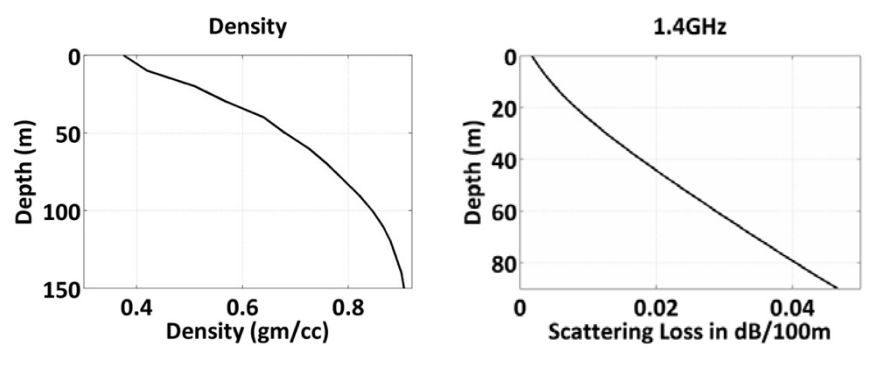


Figure 12: (Left) Density as a function of depth. (Right) Scattering loss (dB/100m) as a function of depth. After Jezek et al. (2015 [RD8]).

By using the above equations and an appropriate temperature profile, it is possible to simulate the TB of the internal part of Antarctica. For example, Figure 13 shows the TB profile (expressed as a cumulative sum of the TB from the bottom to the surface) for different temperature profiles obtained from the Robin model (Van der Veen, 1999) for a given depth (3700 m) and different accumulation rate values that explain the different temperature profiles.

The results show that, for this model, all depths of the ice sheet contribute to the surface TB and confirm that different temperature profiles lead to a different surface TB, as observed in SMOS data. Results obtained from such a simple model demonstrate that this model is reliable for the simulation of static TB in regions where it remains stable in time (i.e. in the internal part of the plateau), where the scattering and the internal reflections between layers are both negligible and the modification of the physical properties of firn layers near to the surface could be disregarded. The Antarctic firn, however, is generally highly layered.

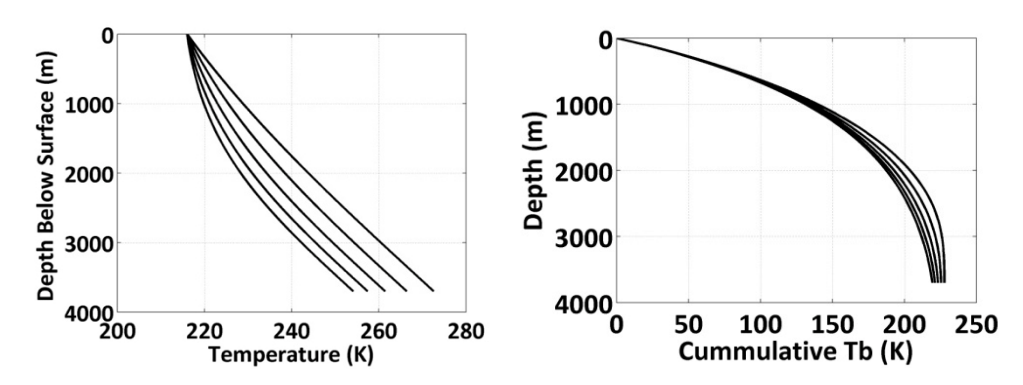


Figure 13: (Left) Modelled temperature profile for different values of accumulation rates to 3700 m depth. The rightmost (warmest profile) is calculated using the lowest accumulation rate of 0.01 m.yr⁻¹, while the 5 curves represent accumulation rates of 0.02, 0.03, 0.04 and 0.05 m.yr⁻¹ (from right to left), respectively. (Right) Cumulative TB found by totaling emissions from the surface to each depth for the family of temperature profiles presented in the left panel. From Jezek et al. (2015 [RD8]).

This simple forward model (without scattering) could serve as a basis for simulations of ice-shelf areas. For that, inputs will include an ice layer with ocean below and some marine ice in-between. For radiative transfer, only one or two ice layers will be assumed, and Mironov et al. (2013) may be used for the ice permittivites.

3.3 Incoherent model

Two main incoherent models are available and are currently used to study microwave frequencies. Both models are based on the radiative transfer theory and are designed to model the microwave emission of layered snowpacks.

DMRT-ML

One of the models considered will be the DMRT model (Dense Media Radiative Transfer) developed under the QCA-CP approximation (Quasi Crystalline Approximation with Coherent Potential) (Tsang et al., 2000). This approach takes into account the coherence of random scatterers, and satisfies the principle of energy conservation. In recent years, the DMRT theory has been implemented by the LGGE

team into a model named DMRT Multi-Layer (DMRT-ML; Picard et al., 2013). The model is written in Fortran90, is well documented, and is available to the snow remote sensing community as an open-source software (http://lgge.osug.fr/\picard/dmrtml/). A convenient user interface is provided in Python.

DMRT-ML describes the snowpack as a multi-layer medium in which each snow layer is characterized by its thickness, temperature, density, grain size, stickiness parameter, and liquid water content. The dense media radiative transfer equation is solved in the form:

$$\cos\theta \frac{d}{dz}\bar{T}_{B}(z,\theta,\phi)$$

$$= -\kappa_{e}\bar{T}_{B}(z,\theta,\phi) + \kappa_{a}T + \int_{0}^{\pi/2} \sin\theta' \,d\theta' \int_{0}^{2\pi} d\phi' \bar{\bar{P}}(\theta,\phi,\theta',\phi') \cdot \bar{T}_{B}(z,\theta',\phi')$$
(11)

The effective dielectric constant is solved by using the first-order quasi-crystalline approximation and the Percus-Yevik approximation for non-sticky grains, i.e. grains without aggregates (Tsang and Kong, 2001). The emission and propagation of radiation throughout the snowpack are computed by using the Discrete Ordinate Method (DISORT; Chandrasekhar, 1960), which takes into account multiple scattering between the layers.

DMRT-ML was primarily developed for microwave frequencies higher than L-band. For example, it was used at Dome C with in-situ snow measurements as input, and was compared to satellite observations at 18.7 and 36.5 GHz (Brucker et al., 2011) or ground-based observations at 11, 19 and 37 GHz (Picard et al., 2013). It was also used in Antarctica to retrieve snow properties from 18.7 and 36.5 GHz observations (Brucker et al., 2011). However, even if this model has been widely used for higher frequencies, its applications to L-band are only recent. Thus, we will need to make a careful check of both the sensitivity and the validity of this model for our studies.

MEMLS

The MEMLS model is an incoherent model that is also based on the radiative transfer theory (Matlzer and Wiesmann 1999; Wiesmann and Matzler 1999). MEMLS uses the six-flux theory to propagate radiation through the different layers. The radiative transfer equation of the TB is:

$$-\frac{dT_{01}}{dz}|\cos\theta| = -\gamma_a(T_{01} - T) - \gamma_b(T_{01} - T_{02}) - \gamma_c(4T_{01} - T_{03} - T_{04} - T_{05} - T_{06})$$
 (12)

In which the horizontal fluxes T_{03} , T_{04} , T_{05} and T_{06} are equal and represent trapped radiation due to total reflection, and the vertical fluxes T_{01} and T_{02} represent downwelling and upwelling radiations within the critical angle, respectively. The absorption coefficient γ_a is derived from the effective permittivity, which is calculated in a similar way to that of equations (6)-(8).

The scattering coefficient γ_b in the backward direction and the coefficient for coupling between the vertical and horizontal fluxes γ_c are related to the total scattering coefficient γ_s through the refractive index n of the layer. It should be mentioned that whereas the DMRT-ML describes the scattering of the media by using the "grain size" parameter, which takes into account the dimensions of particles, MEMLS describes scatterers by using a correlation length parameter so that the snow structure is described by a spatial two-point correlation function. Nevertheless, it has been demonstrated that the exponential correlation length p_{ex} can be related to an effective grain radius a through $p_{ex} = a(1 - f_v)$ under certain assumptions, where f_v is the volume fraction (Matzler, 2002).

The six-flux equations are solved by calculating eigenvalues (damping coefficient) in each layer and unknown coefficients are determined by matching incoherent boundary conditions, with the effective propagation direction θ of the vertical fluxes being corrected by the volume scattering effects and the intermediate reflectivity being modified due to the polarization mixing of volume scattering.

MEMLS treats a thin layer a with one-way phase delay of less than $3\pi/4$ separating two thick layers as coherent. The thin layer is completely replaced by a coherent reflectivity between the two thick layers, while the volume scattering and absorption of the thin layer are ignored. This option must be used with caution as it was developed for thin ice layers embedded in thick snow layers. As "thin" and "thick" are relative to the wavelength, it is quite common that all layers are thin at L-band on the East Antarctic Plateau, where the snow accumulation is ~10cm par annum. A correct treatment of a multi-layer coherent modeling is difficult within the radiative transfer approach.

The results presented in a recent paper demonstrate that if DMRT-ML and MEMLS are run using the same inputs as in the case of the Antarctic Plateau, the simulated TB are very similar (Tan et al., 2015).

3.4 Coherent models

In radiative transfer theory, only the propagation of the incoherent wave is explicitly taken into account while the interference phenomena are ignored. However, interferences within the layers are particularly important when the thickness of the layer is of the order of -or less than- that of the wavelength, which is more pronounced at L-band than at higher frequencies. Another way to perform simulation at L-band is to compute the emission and propagation of waves, instead of the energy flux, in order to explicitly account for interference phenomena. This "coherent approach" is derived from Maxwell's equation, and requires considerable simplification of the medium description in order to be computationally realistic. This alternative has already been used successfully (e.g. Surdyk and Fily, 1995; West et al., 1996).

The most important simplification in this model is to disregard scattering by snow grains. This assumption is usually valid at low frequencies (about < 10 GHz), since the wavelength is several orders of magnitude larger than grain size; however, but extra verification of this assumption is needed everywhere on the continent. Thus, scattering by grains is insignificant in comparison with the absorption and scattering caused by reflections at the interfaces between the layers (Mätzler, 2006 [RD16]).

If the volume scattering effects in the ice sheet are disregarded, the thermal emission problem of a stratified medium has an exact solution with explicit formulas as expressed in Tsang and Kong (1985, 2001). The fluctuation-dissipation theorem connects the thermal motion inside a dissipative medium, resulting in a fluctuating dipole moment with an equivalent current source $\bar{J}(\bar{r},\omega)$ with expectation $\langle \bar{J}(\bar{r},\omega)\bar{J}^*(\bar{r}',\omega')\rangle$. The latter is proportional to $\Theta(\omega,T)\approx KT$ at microwave frequencies, following the Rayleigh-Jeans approximation of Plank's radiation law, where K is the Boltzmann constant, and T is the absolute temperature. The equivalent current source $\bar{J}(\bar{r},\omega)$ generates radiation $\bar{E}(\bar{r},\omega)$ through the dyadic Green's function $\bar{G}(\bar{r},\bar{r}'')$ with multilayer configuration. The TB as a spectral description of the differential radiation power is related to the auto-correlation of the radiation field. By applying a farfield approximation of the dyadic Green's function, a closed form for the TB is obtained:

$$T_{Bv}(\theta_{o}) = \frac{k}{\cos \theta_{o}} \sum_{l=1}^{n} \frac{\varepsilon_{l}''T_{l}}{2\varepsilon_{0}} \frac{(|k_{lz}|^{2} + k_{x}^{2})}{|k_{l}|^{2}}$$

$$\times \left\{ \frac{|C_{l}|^{2}}{k_{lz}''} \left(e^{2k_{lz}''d_{l}} - e^{2k_{lz}''d_{l-1}} \right) - \frac{|D_{l}|^{2}}{k_{lz}''} \left(e^{-2k_{lz}''d_{l}} - e^{-2k_{lz}''d_{l-1}} \right)$$

$$+ \frac{|k_{lz}|^{2} - k_{x}^{2}}{|k_{lz}|^{2} + k_{x}^{2}} \cdot 2Re \left[\frac{C_{l}D_{l}^{*}}{ik_{lz}'} \left(e^{-i2k_{lz}'d_{l}} - e^{-i2k_{lz}'d_{l-1}} \right) \right] \right\}$$

$$+ \frac{k}{\cos \theta_{o}} \frac{\varepsilon_{l}''T_{l}}{2\varepsilon_{0}} \frac{(|k_{lz}|^{2} + k_{x}^{2})}{k_{lz}'|k_{l}|^{2}} |T^{TM}|^{2} e^{-2k_{lz}''d_{l}}$$

$$T_{Bh}(\theta_{o}) = \frac{k}{\cos \theta_{o}} \sum_{l=1}^{n} \frac{\varepsilon_{l}''T_{l}}{2\varepsilon_{0}}$$

$$\times \left\{ \frac{|A_{l}|^{2}}{k_{lz}''} \left(e^{2k_{lz}''d_{l}} - e^{2k_{lz}''d_{l-1}} \right) - \frac{|B_{l}|^{2}}{k_{lz}''} \left(e^{-2k_{lz}''d_{l}} - e^{-2k_{lz}''d_{l-1}} \right) \right.$$

$$+ 2Re \left[\frac{iA_{l}B_{l}^{*}}{k_{lz}'} \left(e^{-i2k_{lz}'d_{l}} - e^{-i2k_{lz}'d_{l-1}} \right) \right] \right\}$$

$$+ \frac{k}{\cos \theta_{o}} \frac{\varepsilon_{l}''T_{l}}{2\varepsilon_{0}} |T^{TE}|^{2} e^{-2k_{lz}''d_{l}}$$

$$(13b)$$

Subscript l denotes the l-th snow/ice layer beneath the air/snow interface, while subscript t denotes the bottom half-space of the sub-glacial media. ε_l'' (ε_t'') and T_l (T_t) are the imaginary part of the permittivity and the physical temperature of the l-th (t-th) layer, respectively. $k_{lz} = \sqrt{k_l^2 - k_x^2}$, $k_l = k\sqrt{\varepsilon_l/\varepsilon_0}$, $k_x = k\sin\theta_o$, where θ_o is the observation angle measured in air. $z = -d_{l-1}$ and $z = -d_l$ are the top and bottom interface of the l-th snow/ice layer. T^{TM} and T^{TE} are the overall transmission coefficients of the layered media for vertical and horizontal polarizations, respectively. A_l and B_l are the upward and downward electric field amplitude coefficients in the l-th layer for the horizontal pol, while C_l and D_l are the upward and downward electric field amplitude coefficients in the l-th layer for the vertical pol. A_l , B_l , C_l and D_l can be determined by using the propagation matrix recursively, as documented in Tsang and Kong (1985, 2001).

With the wave approach, the simulation obtained for a specific snowpack configuration (i.e. a given set of inputs) may differ considerably from those obtained with a slightly different snowpack. This result is due to the high sensitivity of interference phenomena to layer optical depth. To account for the variable nature of the snowpack at the scale of one pixel, it is essential to average a large number of simulations using inputs that represent natural variability. Since thousands of simulations are required, it would be impossible to obtain the input profiles from direct measurements. A stochastic model is used to generate such profiles (examples in West et al., 1996, or in Leduc-Leballeur et al., 2015). The output of the model is the average of TB computed by using all the generated profiles.

The coherent model treats all the wave propagation and reflections in a fully coherent manner, and is thus subject to strong wave interference in a single realization if a fluctuating density profile is assumed. The interference is sensitive to the thickness and density of each layer in which intermediate reflection is significant. The ice layer effective permittivity model previously mentioned is applied in the coherent model.

Recently, two models have been developed that are based on the wave approach from the Tsang and Kong (1985, 2001) equation. The University of Washington implemented a version (Tan et al., 2015)

within the framework of the UWBRAD project (cf. section 5), while the LGGE team implemented another version, called WALOMIS (Wave Approach for LOw-frequency Microwave emission in Snow; Leduc-Leballeur et al., 2015).

3.5 Preliminary results of inter-comparison models

Tan et al. (2015) performed an inter-comparison between the electromagnetic models described above: first order model, DMRT-ML, MEMLS, and coherent model. The authors ran models in a ice sheet stratification similar to the one illustrated in section 3.1 for the Dome-C area in Antarctica. Tests were performed at nadir from 0.5GHz to 2.0GHz for four cases of correlation length l of 3cm, 5cm, 10cm and 40cm. In all cases, a water base was assumed with the warmer ice sheet temperature profile specified by $T_s = 216K$, $M = 0.01m \cdot yr^{-1}$, and H = 3700m in the temperature profile equation. DMRT-ML and MEMLS results were averages over ~150 realizations, while the coherent model was an average of 1000 realizations (to ensure sufficient averaging of the interference effects captured only by the coherent model). TB at nadir with l = 40cm had a maximum standard deviation over the 0.5 - 2.0 GHz spectra of 1.1K for DMRT-ML and MEMLS and of 7.3K for the coherent model. This implied a much smaller number of realizations needed in order to achieve reliable stable results. For l = 3cm, however, the standard deviation could be as large as 2.0K for DMRT-ML and MEMLS and 52.5K for the coherent model, and required a sufficiently large number of realizations for the coherent model to reach stability. The results are depicted in Figure 14.

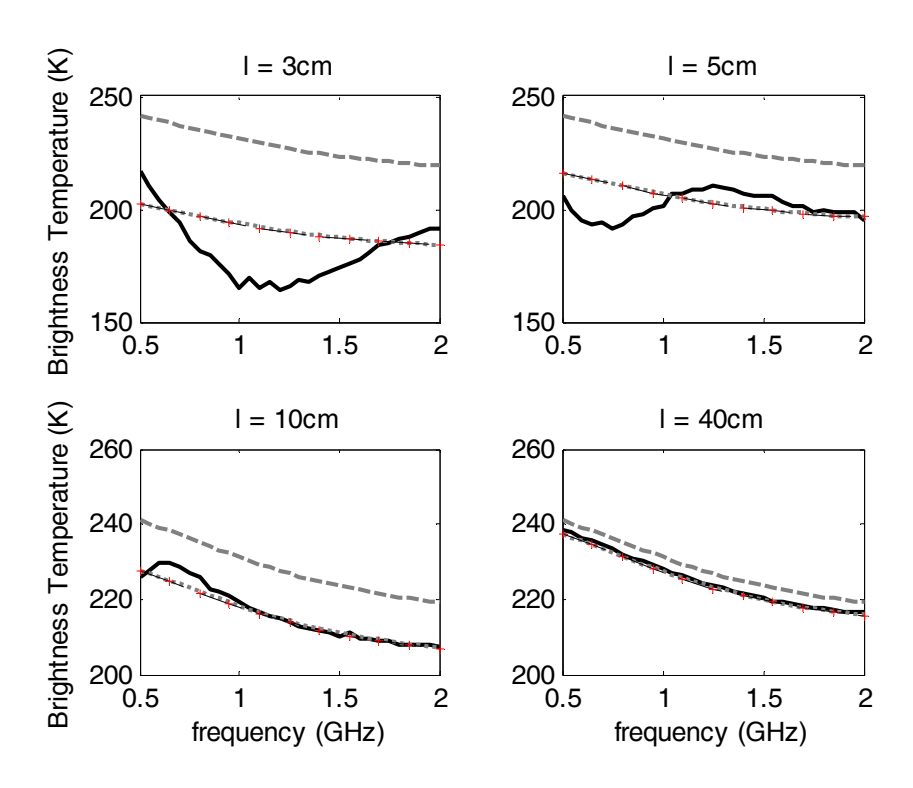


Figure 14: TB of incoherent and coherent models with correlation lengths of density fluctuation of (a) 3cm, (b) 5cm, (c) 10cm and (d) 40cm. The same $\Delta = 0.040\text{g/cm}^3$ and $\alpha = 30m$ are applied to each case assuming a water base. The cloud model is run on the average density profile (grey dashed curve); DMRT-ML (grey dotted curve) and MEMLS (fine black dashed curve with red markers) are run on some $150~(100^{\sim}200)$ realizations of density profile and then averaged. The coherent model is averaged over on 1000~Monte Carlo simulations (black solid curve). Note that the MEMLS and DMRT-ML results are almost identical, and are difficult to distinguish in the figure. Their RMS differences aggregated across all frequencies are 0.23K, 0.32K, 0.30K and 0.34K for the correlation lengths of 3cm, 5cm, 10cm and 40cm, respectively. From Tan et al. (2015).

As expected, the first order model TB were insensitive to correlation length. The other three models showed that the TB dropped significantly as the correlation length decreased. The DMRT-ML and MEMLS results were almost identical. Indeed, if differences were aggregated across all frequencies, the RMS differences between models were 0.23K, 0.32K, 0.30K and 0.34K for the correlation lengths of 3cm, 5cm, 10cm and 40cm, respectively. The maximum difference was less than 0.5K. Especially for the nadir results presented here, this agreement was perhaps not surprising, since similar permittivity models were used, scattering was unimportant, and the Fresnel reflection coefficients were treated identically in the two models. The models then differed only in their solution to the radiative transfer equation. The results indicate that the six-flux approach of MEMLS was a good analog for the Gaussian quadrature approach, for this case. The coherent results agreed with DMRT-ML and MEMLS for profiles with a large correlation length of 40cm. For the smaller correlation lengths of 3cm, 5cm and 10cm, coherent model results showed quite distinct frequency dependencies from the DMRT-ML (and MEMLS) results. The resonance of the coherent results due to wave enhancement / cancellation depended on the correlation length of the density fluctuation. It is worth noting that, close to the SMOS frequency, the coherent and incoherent models agreed fairly independently on the correlation length.

The angular response of the TB of the ice sheet was also calculated by means of DMRT-ML, MEMLS and the coherent model at 1.4GHz, and are compared in Figure 15 for both polarizations by assuming two sets of correlation lengths of 3 and 10 cm, respectively.

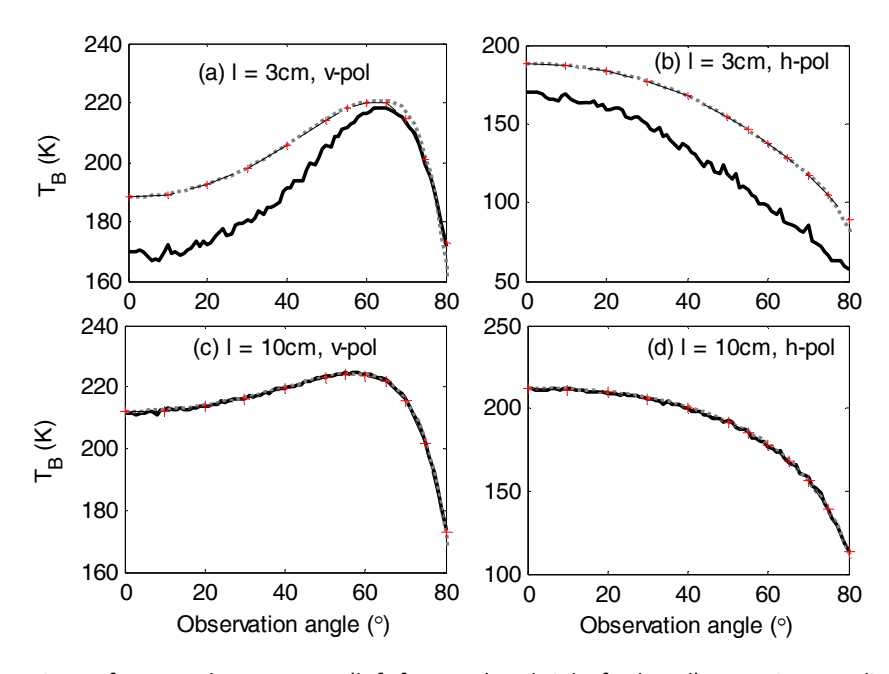


Figure 15: Comparison of TB angular response (left for v-pol and right for h-pol) at $1.4 \mathrm{GHz}$ predicted by DMRT-ML, MEMLS and the coherent model. The TB are shown in (a, b) for l=3cm, and (c, d) for l=10cm. The coherent model results are shown as thick black solid curve; DMRT-ML results are shown as thick grey dotted curve; the MEMLS results are shown as the fine black dashed curve with red marks. Note that the MEMLS and DMRT-ML results are almost identical, and are difficult to distinguish in the figure.

Also here, the figures show that DMRT-ML and MEMLS are almost identical for both correlation lengths. The coherent model results agree closely with DMRT-ML and MEMLS for l=10cm. For l=3cm, when the coherence effects are significant, the coherent model results in v-pol seem to change more rapidly with respect to the observation angle due to phase-enhanced interference.

Lastly, the coherent model results and the DMRT-ML results were compared with the L-band SMOS angular data of Dome C. In this case, the SMOS data were averaged over 4 months between November 2012 and March 2013, for a total of 274 images. The coherent model and the DMRT-ML were calculated on ice sheet profiles with a correlation length of 9 cm leading to a mean layer thickness of 11.54 cm, a damping factor $\alpha=70\text{m}$, and $\Delta=0.040\text{g/cm}^3$ leading to a near surface layer density variation with a standard deviation of 0.045g/cm^3 . These parameters were within the range of the field measurement at Dome C. Again, the coherent and incoherent model results were close as the coherence effects were extinguished at L-band with a correlation length of 9cm. The model predictions also followed the H-pol observations up to 35° with a difference of less than 1.7K. However, as the observation angle continued to increase, the predictions fell below the observations to ~20K at the observation angle of 60°. The higher H-pol TB observed implied an over-estimation of the reflections at large observation angles, which was possibly due to the roughness of the interfaces. The rough interface effects, should this be important, may also disturb the wave phase as it propagates over a long distance.

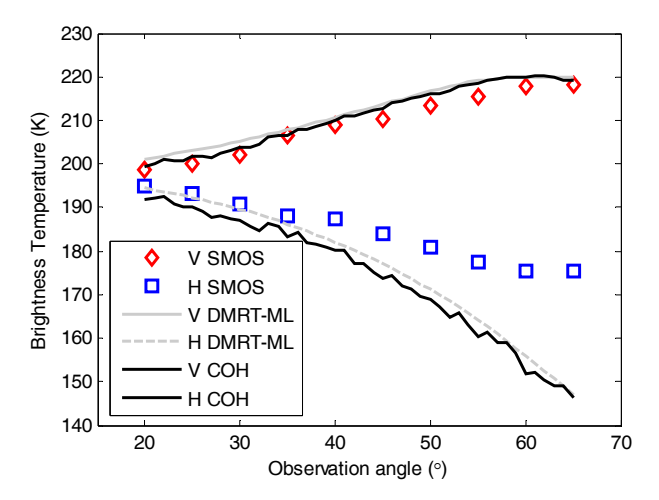


Figure 16: Comparison of TB model prediction from DMRT-ML and the coherent model with L-band SMOS angular data at 1.4GHz. The ice sheet density fluctuation is quantified by l=9cm, $\alpha=70m$, and $\Delta=0.040g/cm^3$.

The results obtained demonstrate that the models were able to represent the SMOS TB and that, for this particular case, the difference between the coherent and incoherent models are negligible, while in other cases it could be relevant. These results must be considered as preliminary, and additional tests and examples must be performed in order to consolidate them.

4 Summary of available associated datasets

4.1 In situ measurements

Almost all of the in-situ datasets of measurements are located in the Dome C area, due to the extensive calibration activities for remote sensing missions (e.g. DOMEX or DomeCAir campaign). Several instruments were installed for monitoring atmospheric and snow parameters. This area will be very useful for detailing exploring L-band signals in the Antarctic ice-sheet. However, at the moment, we have very few in-situ measurement in other areas of Antarctica. This is a big gap in the extension of the analyses, in particular to coastal regions and ice-shelves, where snow properties are very different from those in the Dome C area.

Snow properties in the Dome C area:

Numerous datasets are available, thanks to the in-situ measurements carried out mainly by IFAC and LGGE. Regular temperature, grain size, and density profiles are collected down to a depth of 20 m. Due to the large penetration depth at L-band, snow property measurements in depth are very useful. In this context, LGGE has organised a campaign (with the support of the French polar institute (IPEV)) in order to obtain grain size and density profiles down to a depth of 80 m with a very high resolution of 5 cm. Moreover, a temperature profile has been obtained by LGGE down to bedrock (at 3200 m).

DomeCAir campaign:

The airborne survey DOMECair 2013 and its instrumentation were designed to obtain calibration and validation data for two different satellite missions of ESA's Earth Explorer mission: the SMOS and GOCE satellites. This campaign provided TB in V and H polarisations at 1.4 GHz, as well as gravity measurements.

In order to evaluate the homogeneity of the area near Dome-C, a raster pattern was flown. The area around Concordia was covered by a grid of 11 lines, each of which was 350 km long, separated by 35 km. Thus 350 x 350 km were covered. The altitude above the terrain was roughly 600 m. In addition to the 11 grid lines, a tie line that crossed all the other lines was flown (for inter-comparison purposes). The surroundings of Concordia were covered more intensely by the star pattern. The lines were 100 km long and centred in Concordia. Lstly, circle flights were carried out to examine a potential azimuthal signature. See Kristensen et al. (2013) for details.

DOMEX campaign:

Starting in 2004, different campaigns, called DOMEX-1, DOMEX-2 and DOMEX-3, which are based on the ground based L-band radiometer RADOMEX has been carried out at Dome-C in the East Antarctic Plateau where the Italian-French base of Concordia is located (Macelloni et al., 2006 [RD18]; 2013 [RD19]). The third experiment began in December 2012 and is still ongoing. The main aim of these experiments was to measure the TB of the area at L-band at different time scales (from 1 month up to several years), and thus to assess its temporal stability. In addition, DOMEX data were compared with SMOS and airborne data collected in the same area (Søbjærg et al., 2013 [RD21]). DOMEX data are collected at an incidence angle of 42°, near to the Brewster angle (around 50°).

Microwave and infrared data collected during the experiment, as well as other ancillary information such as the temperature measured by different probes inserted in the snow down to 10 m and density measurements collected in the first meter along the seasons, were available at IFAC and could be used in this project.

Table 4-3: In situ measurements

Description	Туре	Provided/Available
Dome C area	Temperature, density, grain size	LGGE, IFAC
DomeCAir (airborn campaign)	L-Band TB, gravity	DTU
DOMEX	L- and C-Band TB	IFAC

4.2 Satellites datasets

SMOS

SMOS uses out a 2D interferometer to measure the microwave emission of the Earth surface at L-band (1.4 GHz). The spatial resolution is about 40km on average, with ascending/descending orbits at 6am/6pm, respectively (solar local time), at the Equator. It covers the entire Earth surface within 3 days. SMOS data are available since the beginning of 2010. SMOS TB version 620 with recent calibration improvements is also available, and provides users with better quality L-band TB at full polarizations and over a wide range of incidence angles.

ESA level1 C products are in X/Y polarisations (i.e. the coordinates in the antenna frame), organized by half orbits. H and V polarisations are recommended for this project and so a rotation has to be applied. For this, an in-house tools from CESBIO is freely accessible (http://www.cesbio.upstlse.fr/SMOS_blog/?page_id=749). The data are projected on the isea4h9 grid with a regular inter node distance of 15km.

CATDS (Centre Aval de Traitement des Données SMOS) level 3 TB has also been recently reprocessed (version 2.8), with the last improvements taken into account. These TB are already in H and V polarisations, projected on the EASE Grid version 2 (about 25 km resolution), which is the same grid of SMAP data (http://www.catds.fr/; http://www.catds.fr/sipad/startPage.do)

SMAP

SMAP was successfully launched on 31 January 2015. It is equipped with an L-band radiometer (1.41 GHz) with a 40-km spatial resolution, and withnan L-band SAR (1.26 GHz) with a 1-3 km resolution. Both instruments use a parabolic mesh reflector that has a constant incidence angle of 40°. The radiometric uncertainty of the radiometer is expected to be 1.3K. SMAP has a sun synchronous orbit and an equator crossing at 6 AM (descending orbits) and 6 PM (ascending orbits), local solar time.

Data are projected on the EASE Grid version 2, which is an equal-area grid, with a resolution of ~36km for the L-band TB products. The following table is extracted from Das et al. (2014) and presents the different products available from the SMAP mission. A complete description of the SMAP data is provided in Das et al. (2014).

The SMAP data will be delivered by the NASA Distributed Active Archive Center (DAAC) at NSIDC (nsidc.org/data/smap) and also at https://www.asf.alaska.edu/smap/. The release plan is:

- beta L1 products: 6 months after launch,
- beta L2-L4 products: 9 months after launch,
- validated L1 products: 9 months after launch,
- validated L2-L4 products: 15 months after launch.

SMAP MISSION DATA PRODUCTS

Data Product Short Name	Description	Gridding (Resolution)
L1B_S0_LoRes	Low Resolution Radar σ_o in Time Order	(5 × 30 km)
L1C_S0_HiRes	High Resolution Radar σ_o on Swath Grid	1–3 km
L1B_TB	Radiometer T_B in Time Order	(36 × 47 km)
L1C_TB	Radiometer TB on Earth Grid	36 km
L2_SM_P	Half-Orbit Radiometer Soil Moisture	36 km
L2_SM_A	Half-Orbit Radar Soil Moisture	3 km
L2_SM_AP	Half-Orbit Active/Passive Soil Moisture	9 km
L3_FT_A	Daily Global Composite Freeze/Thaw State	3 km
L3_SM_P	Daily Global Composite Radiometer Soil Moisture	36 km
L3_SM_A	Daily Global Composite Radar Soil Moisture	3 km
L3_SM_AP	Daily Global Composite Active/Passive Soil Moisture	9 km
L4_SM	Surface & Root Zone Soil Moisture	9 km
L4_C	Carbon Net Ecosystem Exchange	9 km

Aquarius

Aquarius satellite was launched in June 2011 with the main objective of measuring sea surface salinity. It consists of three L-band radiometers (1.413 GHz) at 3 incidence angles (29.2°, 38.4° and 46.3°), with a resolution of 76 km x 94 km, 84 km x 120 km, and 97 km x 156 km, respectively, and has a radiometric accuracy of 0.2K. Local descending time at the equator is 6 am.

TB H and V are gridded on the EASE Grid version 2, with a spatial resolution of ~36km. Version 4 of the Weekly average TB (level 3) is available on polar grid and is distributed by the NSIDC at http://nsidc.org/data/aq3_tb.html. Also available on the same polar projections are L3 normalized radar cross-section and L3 weekly sea surface salinity.

GOCE

The GOCE mission has provided high-resolution gravity field data at a resolution of 80 km or better (Forsberg et al, 2015). The GOCE data will help to augment the gaps in the current Antarctic BEDMAP2 thickness compilation (Fretwell et al., 2015) by means of an inversion of the gravity field measurements of GOCE to ice thickness. Although this indirect thickness estimate was an official science goal of the GOCE mission, so far no formal update of BEDMAP2 with the final Release-5 GOCE data has been reported. This will be attempted in the present project by using high-resolution GOCE tensor gravity gradient grids for the highest spatial resolution.

MODIS

MODIS (or Moderate Resolution Imaging Spectroradiometer) is a key instrument aboard the Terra (EOS AM) and Aqua (EOS PM) satellites. Terra's orbit around the Earth is timed so that it passes from north to south across the equator in the morning, while Aqua passes south to north over the equator in the afternoon. Terra MODIS and Aqua MODIS are viewing the entire Earth's surface every 1 to 2 days, acquiring data in 36 spectral bands, or groups of wavelengths in the 405-2155 nm (bands 1-19) and 1360-14385 (bands 20-36) ranges.

Surface temperature information will be derived from MODIS data, in particular from the product MOD11C3 V41, which is the land surface temperature obtained by using the most refined MODIS algorithm (https://lpdaac.usgs.gov/products/modis_products_table/mod11c3). The product is ready for use in science applications, and has been already used in Antarctic studies (e.g. Scambos, 2013 NASA Headquarters release No. 13-364).

AMSR-E and AMSR2

AMSR-E instrument (Advanced Microwave Scanning Radiometer – Earth) is a passive microwave radiometer aboard the Aqua satellite. It acquired observation with an incidence angle of 55°, at 6.9, 10.6, 18.7, 36.5 and 89 GHz in vertical and horizontal polarisation from 19 June 2002 to 3 October 2011, and then stopped operating. The National Snow and Ice Data Centre of the United States provided daily TB resampled at different resolution of 12km or 25km. Sea ice concentration and snow depth datasets re-projected on polar grids are also available.

Launched on 18 May 2012 on GCOM-W1 (JAXA) satellite, the AMSR2 instrument is the successor to AMSR-E. Data are available from January 2013.

Sentinel

The Sentinel 1 ESA mission is a constellation of two satellites that share the same orbital plane. Sentinel 1A was launched in April 2014, and Sentinel 1B will be launched in 2016, which improve the revisit time of the observations. This mission carries a synthetic aperture radar (SAR) in C-band which operates in four imaging modes with different resolution (down to 5 m). These data could be used in the coastal area and ice-shelves, as well as the impacted zones, to follow the beginning and end of melt events. Data provided by ESA in free and open access (for details, see https://sentinel.esa.int/web/sentinel/sentinel-data-access).

CryoSat

Surface elevation, elevation changes, and the surface slope have been derived from CryoSat2 (Helm et al., 2014). Data are available on a 25 km grid through the PANGEA database. The uncertainty of the digital elevation model is less than 3±15 m for 80% of the data (based on a comparison with ICESat). CryoSat2 data are best suited to the CRYOSMOS study because they had the same acquisition period.

Table 4-4: Satellite datasets

Description	Туре	Provided/Available
SMOS, Aquarius, SMAP	L-Band TB: total time series and monthly, weekly average	CESBIO, NASA
AMSRE-2	MW TB: total time series and monthly, weekly average	LGGE, IFAC, CESBIO, DTU
CryoSat	Products: slope, surface height	AWI Pangaea
GOCE	Gravity field (spherical harmonic expansions or grids of gravity gradient tensor elements at nominal GOCE altitude)	DTU
MODIS	Optical/IR data	NASA
Sentinel	Active MW data	ESA

4.3 Derived products

BEDMAP2

Bedrock and surface topography can be obtained from the Bedmap2 database (Fretwell et al., 2013), which can be downloaded from https://secure.antarctica.ac.uk/data/bedmap2/. Bedmap2 provides surface elevation, ice-thickness and the sea floor and subglacial bed elevation of the Antarctic south of 60° S. The Bedmap2 ice thickness grid is made by merging 25 million measurements, which are over two orders of magnitude more than the ones used in the previous Bedmap1 version.

Accumulation map from satellite observations

The Arthern et al. (2006) accumulation map was obtained by performing the continuous-part universal kriging (Kitanidis, 1997) of in-situ measurements from 1950 to 2000 period using a background model based on passive microwave observations (AMSR-E and AVHRR) to guide the interpolation. The dataset is given with a spatial resolution of 25km, but the effective resolution of the map is estimated to be about 100 km. Thus, data variability at a smaller scale should be considered with caution. Moreover, values for locations subject to melt may be unreliable. Data are available online: http://www.antarctica.ac.uk//bas_research/data/online_resources/snow_accumulation/

Daily surface melting in Antarctica from satellite observations

From passive microwave radiometer observations, Picard and Fily (2006) retrieved a dataset of daily surface melting in Antarctica. The microwave data are provided by NSIDC in two datasets: SMMR and SSM/I. The product includes the melted/non-melted status of every pixel on the reduced Southern stereographic polar grid for every day since 1st April 1979 with a spatial resolution of 25 km, but the underlying data are at a resolution of about 60 km. This grid is a cropped version of the Southern stereographic polar grid used by NSIDC. The temporal resolution is 1 day (2 days before 1988), and the records have been almost continuous since 1979. More information and datasets are available online: http://www-lgge.obs.ujf-grenoble.fr/~picard/melting/

Climate models

Glaciological data can be obtained from climate models such as the Regional Atmospheric Climate Model - RACMO (Regional Atmospheric Climate Model) which estimates geophysical data such as precipitation and air temperature, and from the Community Ice Sheet Model — CISM (http://websrv.cs.umt.edu/isis/index.php/Main_Page), which provides information on several parameters such as accumulation and ablation rates, basal heat flux, and surface velocity.

The tri-dimensional meteorological model MAR (Modèle Atmosphérique Régional), which was mainly developed at LGGE (PI: H. Gallée), as well as the one-dimensional snow model CROCUS developed at CEN (Centre National de la Neige, France), can provide geophysical data.

Description	Туре	Provided/Available
BEDMAP2	Height, thickness	Online
Climate models: MAR, RACMO2, CROCUS	Snow accumulation, precipitations, etc.	IFAC, LGGE
Arthern et al., (2006) products	Snow accumulation from satellite observations	Online
Picard et al., (2006) products	Days of melt from microwave satellite observations	LGGE

Table 4-5: Derived products

5 Current initiatives related to the project

UWBRAD – NASA (IFAC)

Starting in 2014 NASA, within the Instrument Incubator Program, founded a new project for the retrieval of the internal ice-sheet temperature using microwave sensors. The project, headed by the Ohio State University (OSU) (PI- Prof. J. Johnson), is entitled Ultra-Wideband Software-Defined Microwave Radiometer (UWBRAD). The UWBRAD concept is the result of extensive modeling studies and research activities, including analyses of ESA's 1.4 GHz SMOS data over Antarctica and Greenland. Research and technology development activities have confirmed that relative changes in ice-sheet internal temperature can be gleaned from multi-frequency emission data over the 0.5 to 2 GHz range, and that a multi-frequency radiometer has the potential to separate temperature and electromagnetic properties in the ice sheet thanks to a model-based retrieval approach. Current radiometers operating in the protected portion of L-band provide only partial ice-sheet temperature information because of their single frequency measurements. In contrast, UWBRAD will provide TB in 15 channels over the ultrawideband 0.5-2GHz range and in environments containing radio frequency interference (RFI). To enable operations outside the protected portion of the spectrum, UWBRAD incorporates full bandwidth sampling, with software-defined algorithms to provide real-time detection and mitigation of interference and a cognitive radiometry method for locating and utilizing portions of the RFI-free spectrum. A 0.5-2 GHz antenna commensurate with instrumental and scientific requirements and capable of airborne deployment is also under development. The overall project plan includes completion of the instrument in year two, and its deployment in test flights over Greenland ice sheets in year three, for the validation of the scientific performance. UWBRAD data will enhance the research community's ability to determine the ease with which ice deforms internally and the rate at which the ice sheet flows across its base. It will also enhance the community's ability to compile mean annual temperatures and

to monitor climate change. The study also includes theoretical studies on the microwave emission of the ice sheet using different models. Different teams participating in the project including IFAC-CNR, and this guarantees a mutual benefit for the two projects that will work on similar topics, and also guarantee that the CRYOSMOS team will be informed on other initiatives in progress in the US.

PolarGAP - ESA/NSF (DTU)

The ESA/NSF coordinated flight campaign for gravity, magnetic and ice-penetrating radar measurements over the GOCE polar gap (83.5-90°S), is planned for the 2015/16 field season, pending formal agreements with NSF for logistics support and coordinated US science flights.

SMOS+Sea Ice - UHAM

The SMOS+ Sea Ice project shares methodological similarities, for the problem of the retrieval of sea ice thickness, with the problem of the investigation of ice shelf signatures. This project concerns the SMOS data processing and the emissivity model. Moreover, during the SMOSIce 2014 campaign there were some flights over glaciated parts of Svalbard with the EMIRAD2 switched on. This data may perhaps be used for comparisons within the CRYOSMOS project.

Surface masse balance : Imbie project

The ice sheet mass balance inter-comparison exercise (IMBIE) was established in 2011 as a community effort at reconciling satellite measurements of ice sheet mass balance. IMBIE is a collaboration between scientists supported by the European Space Agency (ESA) and the National Aeronautics and Space Administration (NASA), and contributes to assessment reports of the Intergovernmental Panel on Climate Change (IPCC). IMBIE has led to improved confidence in the measurement of ice sheet mass balance and the associated global sea-level contribution. The improvements were achieved through a combination of ice sheet imbalance estimates developed from the independent satellite techniques of altimetry, gravimetry and the input-output method. In going ahead, IMBIE provides a framework for assessing ice sheet mass balance, and has the explicit aim of widening participation in order to enable the entire scientific community to become involved.

6 References

Abdalati W., Steffen K., 1997. Snowmelt on the Greenland Ice Sheet as Derived from Passive Microwave Satellite Data. Journal of Climate, 10(2):165-175.

Alley R. B., Bolzan J. F., Whillans I. M., 1982, Polar firn densification and grain growth, Annals of Glaciology, 3, 7-11.

Arthern R. J., Winebrenner D. P., Vaughan D. G., 2006, Antarctic snow accumulation mapped using polarization of 4.3-cm wavelength microwave emission, J. Geophys. Res., 111, D06107, doi:10.1029/2004JD005667.

Bingham A. W., Drinkwater M. R., 2000, Recent Changes in the Microwave Scattering Properties of the Antarctic Ice Sheet, IEEE Trans. Geosc. Rem. Sens., vol. 38, no. 4, pp. 1810-1820.

Blume H. J. C., Kendall B. M., Fedors J. C., 1978, Measurement of ocean temperature and salinity via microwave radiometry, Boundary-Layer Meteorology, 13(1-4), 295-308.

Brogioni M., Pettinato S., Montomoli F., Macelloni G., 2014, Snow layering effects on L-band passive Measurements at Dome C-Antarctica, Microwave Radiometry and Remote Sensing of the Environment (MicroRad), 13th Specialist Meeting on, Pasadena, CA, USA

Brogioni M., Rahmoune R., Macelloni G., 2013, Characterization of the spatial and temporal stability of East-Antarctic plateau using SMOS data. IEEE TGRS – IGARSS 2013.

Brucker L., Picard G., Fily M., 2010, Snow grain-size profiles deduced from microwave snow emissivities in Antarctica, Journal of Glaciology, 56(197), 514-526.

Brucker L., Picard G., Arnaud L., Barnola J. M., Schneebeli M., Brunjail H., Lefebvre E., Fily, M., 2011, Modeling time series of microwave TB at Dome C, Antarctica, using vertically resolved snow temperature and microstructure measurements, J. Glaciol., vol. 57, no. 201, pp. 171–182.

Brucker L., Dinnat E. P., Koenig L. S., 2014b. Weekly gridded Aquarius L-band radiometer/scatterometer observations and salinity retrievals over the polar regions — Part 2: Initial product analysis, The Cryosphere, 8:915-930, www.the-cryosphere.net/8/915/2014, doi:10.5194/tc-8-915-2014.

Brucker L., Dinnat E. P., Koenig L., 2014a, Weekly gridded Aquarius L-band radiometer/scatterometer observations and salinity retrievals over the polar regions – Part 1: Product description, The Cryosphere, 8: 905-913, www.the-cryosphere.net/8/905/2014, doi:10.5194/tc-8-905-2014.

Brucker L., Dinnat E., Koenig L., 2014, Aquarius L3 Weekly Polar-Gridded TB and Sea Surface Salinity. Version 4. Boulder, Colorado USA: NASA National Snow and Ice Data Center Distributed Active Archive Center (http://dx.doi.org/10.5067/Aquarius/AQ3_TB.004).

Brucker L., Dinnat E.P., Picard G., Champollion N., 2014c, Effect of Snow Surface Metamorphism on Aquarius L-Band Radiometer Observations at Dome C, Antarctica, IEEE Transactions on Geoscience and Remote Sensing, 52(11): 1-10, doi: 10.1109/TGRS.2014.2312102.

Cabot F, Anterrieu E., Kerr Y. H., 2014, A method to inter-calibrate orbiting I-band radiometer, Microrad Final Program, 13th Specialist Meeting on Microwave Radiometry and Remote Sensing of the Environment, Pasadena (California, USA), March 24-27, 2014.

Cao C., Ungar S., Lecomte P., Fox N., Xiong X., Henry P., Buck C., Stenssas G., Zhan X., Campbell P., 2009, Toward consistent satellite calibration and validation for GEOSS interoperability. Geoscience and Remote Sensing Symposium, 2008. IGARSS 2008 I300-I303, doi:10.1109/IGARSS.2008.4778853

Chandrasekhar S., 1960, Radiative Transfer. New York, NY, USA: Dover.

Craven M., et al., 2009, Properties of a marine ice layer under the Amery Ice Shelf, East Antarctica. Journal of Glaciology, 55(192): 717-728.

Das N.N., Entekhabi D., Njoku E.G., Shi J.J.C., Johnson J.T., Colliander A., 2014, Tests of the SMAP Combined Radar and Radiometer Algorithm Using Airborne Field Campaign Observations and Simulated Data, Geoscience and Remote Sensing, IEEE Transactions on, 52(4):2018-2028, doi: 10.1109/TGRS.2013.2257605

Depoorter M. A., Bamber J. L., Griggs J. A., Lenaerts J. T. M., Ligtenberg S. R. M., van den Broeke M. R., Moholdt G., 2013, Calving fluxes and basal melt rates of Antarctic ice shelves, Nature, doi:10.1038/nature12567

Eagleman J. R., Lin W. C., 1976, Remote sensing of soil moisture by a 21-cm passive radiometer, J. Geophys. Res., 81(21), 3660–3666, doi:10.1029/JC081i021p03660.

Forsberg R., 2014, GOCE and Antarctica, Keynote presentation, Proceedings, ESA GOCE workshop, Paris, Nov 2014, in print.

Fretwell P., Pritchard H. D., Vaughan D. G., Bamber J. L., Barrand N. E., Bell R., Bianchi C., Bingham R. G., Blankenship D. D., Casassa G., Catania G., Callens D., Conway H., Cook A. J., Corr H. F. J., Damaske D., Damm V., Ferraccioli F., Forsberg R., Fujita S., Gim Y., Gogineni P., Griggs J. A., Hindmarsh R. C. A., Holmlund P., Holt J. W., Jacobel R. W., Jenkins A., Jokat W., Jordan T., King E. C., Kohler J., Krabill W., Riger-Kusk M., Langley K. A., Leitchenkov G., Leuschen C., Luyendyk B. P., Matsuoka K., Mouginot J., Nitsche F. O., Nogi Y., Nost O. A., Popov S. V., Rignot E., Rippin D. M., Rivera A., Roberts J., Ross N., Siegert M. J., Smith A. M., Steinhage D., Studinger M., Sun B., Tinto B. K., Welch B. C., Wilson D., Young D. A., Xiangbin C., Zirizzotti A., 2013, Bedmap2: improved ice bed, surface and thickness datasets for Antarctica, The Cryosphere, 7, 375-393, 2013, doi:10.5194/tc-7-375-2013

Fréville H., Brun E., Picard G., Tatarinova N., Arnaud L., Lanconelli C., Reijmer C., van den Broeke M., 2014, Using MODIS land surface temperatures and the Crocus snow model to understand the warm bias of ERA-Interim reanalyses at the surface in Antarctica, The Cryosphere, 8, 1361–1373.

Gow A. J., 1971, Depth-Time-Temperature Relationships of Ice Crystal Growth in Polar Glaciers, USA Cold Regesions Res. Eng. Lab., Hanover, NH, USA, CRREL Res. Rep. 300.

Hall D. K., Comiso J. C., DiGirolamo N. E., Shuman C. A., Box J. E., Koenig L. S., 2013, Variability in the surface temperature and melt extent of the Greenland ice sheet from MODIS, Geophys. Res. Lett., 40, 2114–2120, doi:10.1002/grl.50240

Helm V., Humbert A., Miller H., 2014, Elevation and elevation change of Greenland and Antarctica derived from CryoSat-2, The Cryosphere, 8: 1539-1559, doi:10.5194/tc-8-1539-2014.

Jezek K., Johnson J., Aksoy M., 2012, Radiometric approach for estimating relative changes in intra-glacial average temperature, EOS Supplement, 2012 Fall AGU meeting.

Klein L., Swift C., 1976, An improved model for the dielectric constant of sea water at microwave frequencies, IEEE J. Ocean Eng., OE-2, 104–111.

Kristensen S. S., Søbjærg S.S., Balling J. E., Skou N., 2013, DOMECair Campaign, EMIRAD Data: Presentation and Analysis, DTU Space report, 12/11 – 2013, 118 p.

Lagerloef G. et al., 2008, The Aquarius/SAC-D Mission: Designed to meet the salinity remote-sensing challenge, Oceanography, vol. 21, no. 1, pp. 68–81.

Leduc-Leballeur M., Picard G., Mialon A., Arnaud L., Lefebvre E., Possenti P., Kerr Y., 2015, Modeling L-band TB at Dome C, Antarctica and comparison with SMOS observations, IEEE Trans. on Geoscience and Remote Sensing, 53(7), 4022-4032.

Long D. G., Drinkwater M. R., 2000, Azimuth Variation in Microwave Scatterometer and Radiometer Data over Antarctica, IEEE Trans. Geosci. Remote Sens., 38, 4, 1857-1870.

Maaß N., Kaleschke L., Tian-Kunze X., Mäkynen M., Drusch M., Krumpen T., Hendricks S., Lensu M., Haapala J., Haas C., 2015, Validation of SMOS sea ice thickness retrieval in the northern Baltic Sea. Tellus A, 67. doi:http://dx.doi.org/10.3402/tellusa.v67.24617

Macelloni G., Brogioni M., Pampaloni P., Cagnati A., 2007, Multi-frequency Microwave Emission from the East Antarctic Plateau:Temporal and Spatial Variability, IEEE Trans. Geosci. Remote Sensing (Microrad 08, Special Issue), vol. 43, 2029-2039.

Magand O., Picard G., Brucker L., Fily M., Genthon C., 2008, Snow melting bias in microwave mapping of Antarctic snow accumulation. The Cryosphere, 2, 109-115.

Mironov V.L., De Roo R.D., Savin I.V., 2010, Temperature-Dependable Microwave Dielectric Model for an Arctic Soil, Geoscience and Remote Sensing, IEEE Transactions on, 48(6): 2544-2556, doi: 10.1109/TGRS.2010.2040034

Oerlemans J., Cornelis J. van der Veen., 1984, Ice sheets and climate. 21(7), Dordrecht: Reidel.

Picard G., Brucker L., Roy A., Dupont F., Fily M., Royer A., Harlow C., 2013, Simulation of the microwave emission of multi-layered snowpacks using the dense media radiative transfer theory: the dmrt-ml model, Geosci. Model Dev., 6(4): 1061–1078.

Picard G., Brucker L., Fily M., Gallée H., Krinner G., 2009, Modeling time series of microwave brightness temperature in Antarctica, Journal of Glaciology, 55(191), 537-551.

Picard G., Fily M., 2006, Surface melting observations in Antarctica by microwave radiometers: correcting 26 year-long timeseries from changes in acquisition hours, Remote Sensing of Environment, 104 (3): 325-336.

Picard G., Fily M., Gallee H., 2007, Surface melting derived from microwave radiometers: a climatic indicator in Antarctica. Annals of Glaciology, 46: 29-34.

Picard G., Royer A., Arnaud L., Fily M., 2014, Influence of meter-scale wind-formed features on the variability of the microwave brightness temperature around Dome C in Antarctica, The Cryosphere, 8, 1105-1119, doi:10.5194/tc-8-1105-2014

Ricker R., Hendricks S., Helm V., Skourup H., Davidson M., 2014, Sensitivity of CryoSat-2 Arctic sea-ice freeboard and thickness on radar-waveform interpretation, The Cryosphere, 8: 1607-1622, doi:10.5194/tc-8-1607-2014.

Schwank M., Rautiainen K., Mätzler C., Stähli M., Lemmetyinenb J., Pulliainen J., Vehviläinen J., Kontub A., Ikonen J., Ménard C. B., Drusch M., Wiesmann A., Wegmüller U., 2014, Emission of a snow-covered ground with focus on I-band, Remote Sensing of Environment, 154,180-191.

Skou N., Kristensen S. S., Søbjærg S. S., Balling J., 2014, Mapping of the Dome-C Area in Antarctica by an Airborne L-band Radiometer, Proceedings of IGARSS 2014, 3610 – 3613.

Skou N., Kristensen S. S., Søbjærg S. S., Balling J., 2013, DOMECair: An Airborne Campaign in Antarctica Supporting SMOS Calibration, Proceedings ESA Living Planet Symp., Edinburgh, September 2013, 8p.

Stogryn A., 1971, Equations for calculating the dielectric constant of saline water, IEEE Trans. Microwave Theory Tech., vol. MTT-19, 733-736.

Surdyk S., Fily M., 1995, Results of a stratified snow emissivity model based on the wave approach: application to the Antarctic ice sheet, Journal of Geophysical Research: Oceans, 100(C5), 8837-8848.

Tan S., Aksoy M., Brogioni M., Macelloni G., Durand M., Jezek K. C., Wang T.-L., Tsang L., Johnson J. T., Drinkwater M. R., Brucker L., 2015, Physical Models of Layered Polar Firn Brightness Temperatures From 0.5 to 2 GHz, IEEE J. of Selected Topics in Applied Earth Observations and Remote Sensing.

Tian-Kunze X., Kaleschke L., Maaß N., Mäkynen M., Serra N., Drusch M., Krumpen T, 2014, SMOS-derived thin sea ice thickness: algorithm baseline, product specifications and initial verification, The Cryosphere, 8, 997-1018, doi:10.5194/tc-8-997-2014.

Timmermann R et al., 2010, Antarctic ice sheet topography, cavity geometry, and global bathymetry (RTopo 1.0.5-beta). doi:10.1594/PANGAEA.741917, Supplement to: Timmermann R., Le Brocq A. M., Deen T. J., Domack E. W., Dutrieux P., Galton-Fenzi B., Hellmer H. H., Humbert A., Jansen D., Jenkins A., Lambrecht A., Makinson K., Niederjasper F., Nitsche F.-O., Nøst O. A., Smedsrud L. H., Smith W., 2010, A consistent dataset of Antarctic ice sheet topography, cavity geometry, and global bathymetry. Earth System Science Data, 2(2), 261-273, doi:10.5194/essd-2-261-2010

Torinesi O., Fily M., Genthon C., 2003, Variability and Trends of the Summer Melt Period of Antarctic Ice Margins since 1980 from Microwave Sensors. J. Climate, 16, 1047–1060.

Tsang L., Kong J. A., 2001, Scattering of Electromagnetic Waves, 3, Advanced Topics. Wiley Interscience.

Tsang L., Kong J. A., Ding K. H., Ao C., 2000, Scattering of electromagnetic waves, 2, numerical solutions, Wiley Interscience, New York, 705 pp.

Ulaby F. T., Bengal T. H., Dobson M. C., East J. R., Garvin J. B., Evans D. L., 1990, Microwave Dielectric Properties of Dry Rocks, IEEE Trans. Geos. Rem. Sens., 28(3):325-336.

Van der Veen J., Fundamentals of Glacier Dynamics. Rotterdam: A. A. Balkema, pp. 462, 1999.

Wan Z., 2014, New refinements and validation of the collection-6 MODIS land-surface temperature/emissivity product, Remote Sens. Environ., 140, 36–45.

West R. D., Winebrenner D. P., Tsang L., Rott H., 1996, Microwave emission from density-stratified Antarctic firn at 6 cm wavelength, J. Glaciol., 42(140): 63–76.

Zwally H. J., 1977, Microwave emissivity and accumulation rate of polar firn, J. Glaciol., 18(79):195-215.